

University of Naples Federico II



Dispensing pico droplets by pyroelectrohydrodynamic jetting: simulations and experimental results

Department of Chemical, Materials and Production Engineering

Supervisor:
Prof. Pier Luca Maffettone

Advisors:
Prof. Gaetano D'Avino
Dr. Simonetta Grilli

Candidate:
Anna Faraone
Matr. P16000026

ACADEMIC YEAR 2018-2019

Introduction	4
CHAPTER 1	6
PYRO-ELECTRO-HYDRO-DYNAMIC EFFECT	6
1.1 The microfluidics aid	6
1.2 Pyro-Electro-Hydro-Dynamic effect	9
1.2.1 Pyroelectricity	10
1.2.2 Electro-Hydro-Dynamic effect	11
1.2.3 The combined effect (Pyro-EHD)	12
1.2.4 Dispenser improvement	15
1.2.5 Forward pyro-electrohydrodynamic printing	18
CHAPTER 2	20
DROPLET DYNAMICS THROUGH AN ORIFICE	20
2.1 Acting forces	20
2.2 Droplet and surface properties	21
CHAPTER 3	24
MATERIALS AND METHODS	24
3.1 Simulations	24
3.2 SensApp set-up	28
3.2.1 Heat transfer devices	30
CHAPTER 4	32
RESULTS	32
4.1 Device geometry	32
4.1.1 Droplet meniscus shape as a function of the geometry	34
4.1.2 P-jet test in orifice	46
4.2 Droplet formation	51
4.2.1 Printing pin geometry	52
4.2.2 Simulations	53
4.2.3 Experimental tests	55
4.2.4 Wettability tests	59
CHAPTER 5	61
CONSLUSIONS AND PERSPECTIVES	61
References	63

Introduction

This thesis work arises from a collaboration between University of Naples Federico II and the Institute of Applied Sciences and Intelligent Systems belonging to National Council of Research (CNR-ISASI) on a European project, ***SensApp*** (grant agreement No 829104), financed by the European Union's Horizon 2020 research and innovation programme.

The project, in which six partners are involved (**CNR**, Vrije Universiteit Brussel *VUB*, Johannes Kepler University Linz *JKU*, Technical Research Centre of Finland *VTT*, Centro Neurolesi Pulejo Messina, Ginolis *GIN*), has the aim to develop a super-sensor device able to give an early diagnosis of the Alzheimer's disease by a simple blood test.

The Alzheimer's disease (AD) is a progressive and irreversible neurodegenerative disorder, which leads to death. It represents the main cause of dementia in the elderly population, with a great socio-economic impact in the worldwide community. Estimates vary, but experts evaluated that nowadays around 30 million of people are affected by AD and, taking into account the increase of life expectation, this community is likely to rise to about 150 million people by 2050. The current guidelines for clinical diagnosis of AD establish the determination of specific protein biomarkers (Amyloid-beta, tau, P-tau) in cerebrospinal fluid (CSF) through ELISA¹ kit and positron emission tomography (PET) of the brain with amyloid tracer. However, PET is highly expensive and not always available in clinics and lumbar puncture for CSF collection is an extreme invasive intervention that requires hospitalization and hinders follow-up programs during therapies. Nowadays the traditional ELISA kits cannot determine such biomarkers in peripheral blood due to their abundance well below the standard sensitivity that is of 50-100 pg/mL. Therefore, by the time it is recognized, the disease has been progressing for many years. In this framework an early diagnosis of AD is crucial for saving lives.

SensApp aims at developing a super-sensor system that, pushing the sensitivity well below 1 pg/mL, will be able to detect the AD biomarkers (Amyloid-beta, tau, P-tau) in human plasma, thus overcoming the limits of

detection usually encountered by standard ELISA protocols. This super-sensor will enable in future a faster and non-invasive early diagnosis of AD simply through a routine blood test, thus opening the route to highly efficient screening programs among the population².

The contribution of this thesis work is to give reliable dimensions and geometry shape for the device channel, region in which the blood sample will be loaded, by simulating the dynamics of fluid through an orifice in order to choose the size giving thinner drop meniscus shape. Subsequently laboratory tests have been performed to have a comparison between simulated and realistic results and to study the fluid behaviour under the electric field.

Therefore, the elaborate is so structured: a state of art regarding microfluidics aid, ink-jet printing devices, pyro-electro-hydro-dynamic effect and droplet dynamics through an orifice introduces the investigation, then the mathematical model for dynamics simulation is explained, finally simulation and experimental results are presented with relative considerations.

CHAPTER 1

PYRO-ELECTRO-HYDRO-DYNAMIC EFFECT

There is rapidly increasing research interest focused on manipulating and dispensing tiny droplets in nanotechnology and biotechnology so a continuously-increasing demand for specific tools for the deposition of ultra-small quantities of materials at predefined locations has emerged. The ability to fabricate complex microfluidic architectures has allowed scientists to create new experimental formats for processing ultra-small analytical volumes in short periods and with high efficiency. The development of such microfluidic systems has been driven by a range of fundamental features that accompany miniaturization. These include the ability to handle ultra-small analytical volumes, reduced reagent consumption, high efficiency, ultra-low fabrication costs, reduced analysis times, enhanced operational flexibility, integrate functional components within complex analytical schemes and increased instrument portability.

1.1 The microfluidics aid

Microfluidics can be divided in many branches among which we can cite: continuous flow microfluidics and digital microfluidics. The first is characterized by constant, regular, continued flow flowing in closed channels. Continuous flows of liquid are pumped by either mechanical or electrokinetic means and changes of the pressures or electrode voltages are allowed. It allows to manipulate the continuous flow of liquid through microchannels thanks to devices such as external pressure pumps or integrated mechanical micropumps.

Then digital microfluidics, also called droplet microfluidics, is a relatively recent technology for liquid manipulation, which allows the control of discrete droplets on a planar surface, through the use of electric, magnetic, optic or acoustic forces. Digital microfluidics shows a clear analogy with traditional benchtop protocols, and a wide range of established chemical protocols can seamlessly be transferred to a picolitre to nanolitre droplet format. Digital microfluidics (DMF) includes all the standard advantages of conventional microfluidics, furthermore, it offers additional advantages, such as: precise control over unit droplets, easy integration with measurement techniques, multiplex assay capability and there is no need for propulsion devices. A DMF device set-up depends on the substrates used, the electrodes, the configuration of those electrodes, the use of a dielectric material, the thickness of that dielectric material, the hydrophobic layers, and the applied voltage³. A common substrate used in this type of system is glass. Depending if the system is open or closed, there would be either one or two layers of glass. The bottom layer of the device contains a patterned array of individually controllable electrodes. The dielectric layer is found around the electrodes in the bottom layer of the device and is important for building up charges and electrical field gradients on the device. A hydrophobic layer is applied to the top layer of the system to decrease the surface energy in which the droplet will actually be in contact with. The applied voltage activates the electrodes and allows changes in the wettability of droplet on the device's surface. In order to move a droplet, a control voltage is applied to an electrode adjacent to the droplet, and at the same time, the electrode just under the droplet is deactivated.

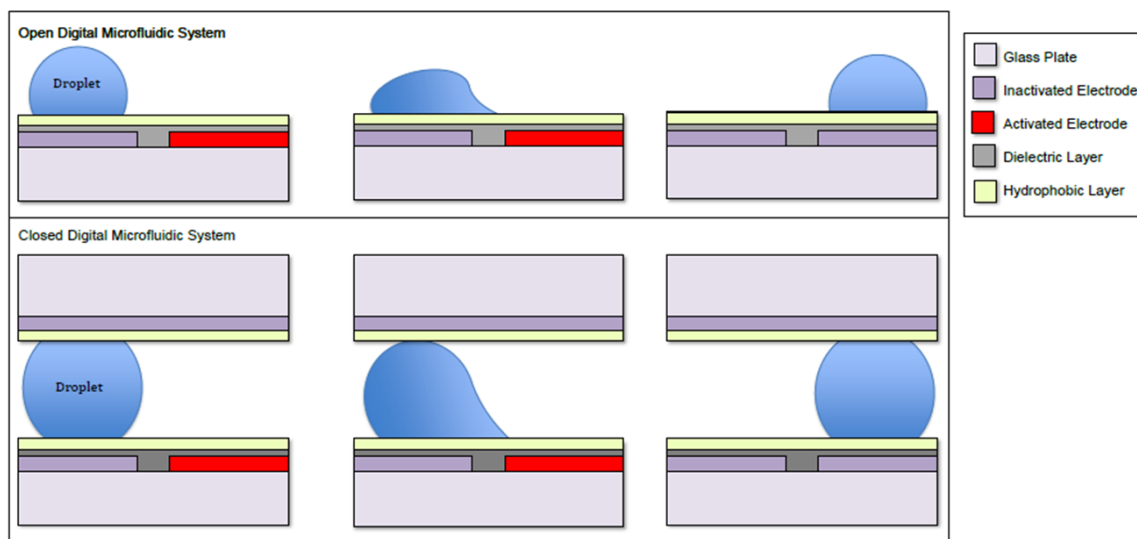


Figure 1 | Digital microfluidics device set-up.

Based on this configuration, different dispensing methods have been developed.

For example, some approaches make use of electrohydrodynamic jetting, which involves a tube with a meniscus bearing a Taylor cone profile spraying a fine jet; other are based on pulsed electrohydrodynamic liquid jetting to obtain droplets on -demand with sizes much smaller than that of the delivery nozzle; or microcapillary nozzles to have high resolution electrohydrodynamic jet printing; or again drop-on-demand printing of conductive ink has been obtained by the application of electrostatic fields. All these electrohydrodynamic techniques provide submicrometre droplets and have the flexibility to pattern fragile organics or biological materials by application of electric potential between the nozzle and the substrate for droplet generation.

The field leads to accumulation of the mobile ions in the liquid near the surface. Electrostatic interaction between ions creates the conical shape of the meniscus, known as a “Taylor cone”. The droplets eject from the cone when the electrostatic stresses overcome the surface tension.

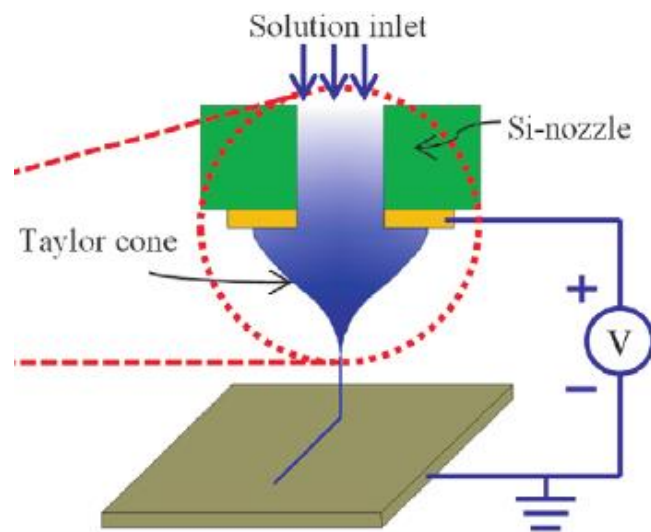


Figure 2| Schematic diagram of the electrohydrodynamic printing system with a nozzle.

Three features of EHD-jet printing allow achieving the high resolution operation: (1) the inner diameter of the nozzles can reach 100 nm, which is much smaller than in the inkjet printing; (2) EHD-jet generated droplets can be significantly smaller than the nozzle diameter; (3) electric field focusing decreases the lateral variations of the droplet positions⁴.

However, these devices require the arrangement of appropriate electrodes and high-voltage circuits. Moreover, the fabrication of the capillary nozzles is very sophisticated and may be subject to cross contamination.

1.2 Pyro-Electro-Hydro-Dynamic effect

Recently, a new approach for liquid dispensing and patterning exhibiting the pyroelectrohydrodynamic effect has been demonstrated. It has the advantages of being electrode-less and nozzle-less, and furthermore using this method liquid printing with attoliter drops resolution has been obtained.

In order to understand how this system works it is well to explain some concepts related to pyro-EHD functioning.

1.2.1 Pyroelectricity

Pyroelectricity is a property of particular materials which exhibit a spontaneous polarization that depends on the temperature ⁵. This property depends on the molecular structure of the material: a pyroelectric solid has inner dipoles, due to the presence of cations or anions in the structure ⁶. In equilibrium conditions (constant temperature), each dipole has its orientation and the total electric dipole moment is zero. A temperature variation induces a movement between the atoms (which have a certain mobility) and, for that reason, a change in the dipoles strength (therefore, the polarity⁷) and, consequentially, a charge displacement on the material surface, i.e. an electric current. It is important to underline that, if the material remains at the same temperature, after it has undergone to a thermal variation, the inner domains work to recover an equilibrium, crowding the charges on the external surfaces, reinstating the starting polarization and setting to zero the electric field. That means just a thermal gradient is able to induce an electric current ^{6,8}. It could be compared to a thermoelectrical material that, once heated, produces an electric current and a stable electrical potential, due to the inner displacement of electrons and holes⁹, but a pyroelectric material attracts electrons from the external ambient, in order to compensate the exceed of charges occurred on the surface⁶.

A pyroelectric material can be either a ceramic, a polymer or a crystal. Between crystals there is Lithium Niobate (LiNbO_3 ¹⁰) on which the interest has been focused.

1.2.2 Electro-Hydro-Dynamic effect

The electrohydrodynamic effect consists of charge displacement induced in the liquid due to the electric field that employs attractive and repulsive forces with the liquid molecules ^{11, 12} . The result consists on the deformation of the liquid drop that assumes a conical shape, known as Taylor's cone ¹³ (Fig.3), due to a charges accumulation at the interface ¹⁴ .

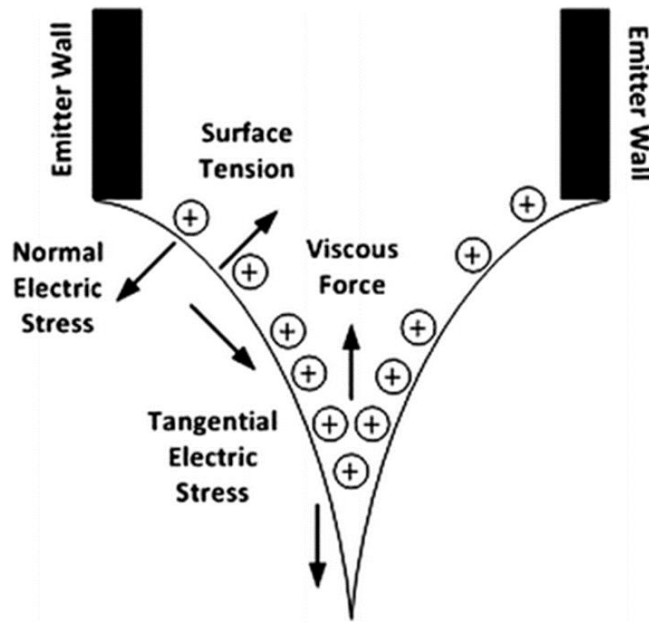


Figure 3 | Taylor's cone. Distribution of charges during Taylor's cone formation.

In particular, Taylor's cone is an equilibrium condition mediated by the forces generated by the surface tension force and the external electric force density ¹³ . In other words, an equivalence between a term $F\gamma$, relative to the surface tension contribute, and a term Fe , relative to the electric external stimulus, has to be reached ¹⁵ .

1.2.3 The combined effect (Pyro-EHD)

If the electric field that activates the EHD phenomenon is generated by a pyroelectric crystal, the combined effect is defined pyro-electro-hydro dynamics (pyro-EHD^{16, 17}) and allows to manipulate liquids or polymeric solution without the use of electrodes. In Fig.4 the set-up realized for classic pyro-EHD printing is reported:

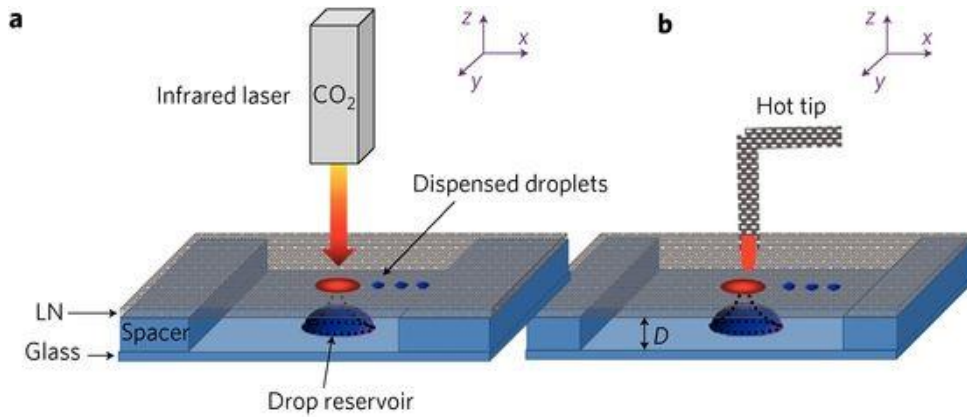


Figure 4| Pyroelectrohydrodynamic dispenser. **a.** Microfluidics device heated with infrared laser. **b.** with hot tip of soldering iron.

The system is constituted by two plates and a heat source. The heat sources

could be a non-contact infrared beam (continuous-wave CO₂ laser emitting at 10.6 mm) or a hot tip of a conventional soldering iron, acting as a contact stimulus (Fig. 1a, b). A microscope glass slide forms the base of the liquid reservoir (which could be a drop or a film), and the LN crystal wafer (z-cut, optically polished and 500 mm thick) acts as an auxiliary plate that drives the process and acts as a substrate for the dispensed liquids. A pointwise thermal stimulus is applied to the LN crystal to induce the pyroelectric effect locally (the maximum operation temperature of the hot tip is ~250°C). At equilibrium, the spontaneous polarization P_s of the LN crystal is fully compensated by the external screening charge, and there is no electric field¹⁸. According to the pyroelectric effect, the temperature change ΔT causes a variation ΔP_s , which builds up an electric potential across the z surfaces. Neglecting the losses, a surface charge

density $\sigma = P_c \Delta T$ appears locally when the tip heats the crystal, where P_c is the pyroelectric coefficient.

The dispensing is guided by the pyroelectric field that induces a charge displacement on the liquid surface; the reservoir drop turns into a Taylor's cone^{19, 20} shape, until the attractive (or repulsive) force exerted toward the crystal gets start the dispensing of drops or fibers, in order to produce drops arrays or patterns.

For a fixed drop volume, a critical value D_c for the distance D between the base and the substrate can be defined according to the following equation²¹:

$$D_c = (1 + \vartheta/4)V^{1/3}$$

where ϑ is the contact angle and V the volume drop reservoir. If $D < D_c$ a stable liquid bridge is established (Fig. 5a) if, instead, $D > D_c$ a stable liquid bridge cannot be established between the plates and a liquid stream regime occurs (Fig.5 b, c)¹⁶.

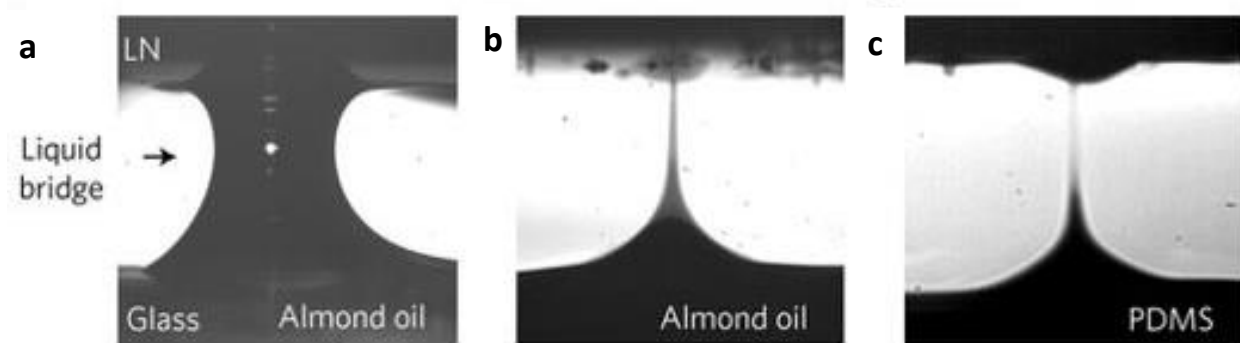


Figure 5| Pyroelectrohydrodynamic dispensing. a, Liquid bridge obtained when D is shorter than the critical distance. e, f, shooting of almond oil and PDMS (PDMS has a continuous blasting cone due to its higher viscosity).

This instability is interesting to break up the liquid reservoir and to dispense droplets.

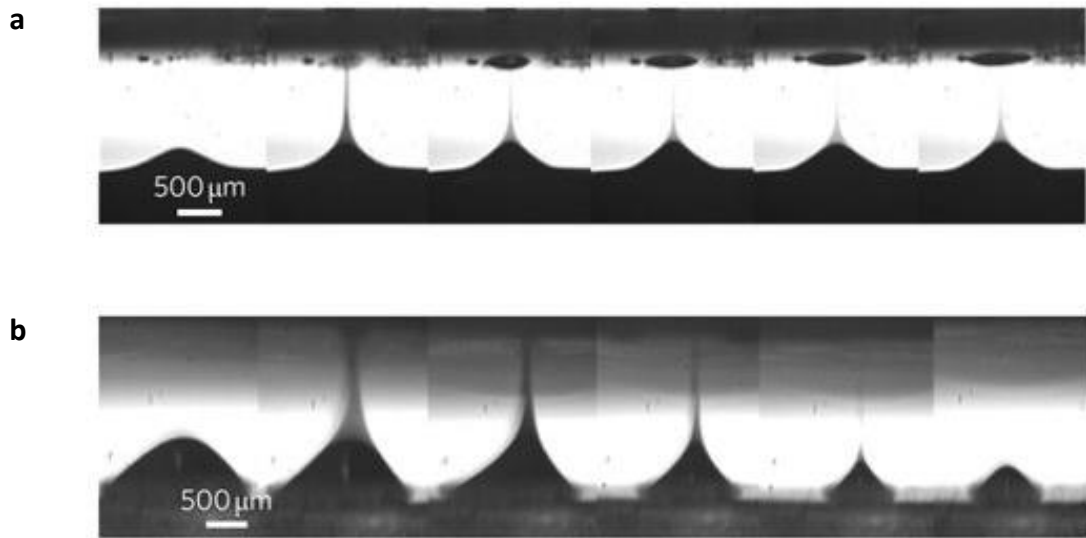


Figure 6| Dispensed sequences. Sequence of almond oil shots taken from a film stimulated by hot tip (a) and from a sessile drop stimulated by IR laser (b).

In figure 6 are reported two sequences of liquids shooting for a film stimulated by a hot tip (Fig. 6a) and by infrared laser pulses (Fig. 6b). The dynamic evolutions show that the reservoir first deforms into a conical tip, with a height that increases under the pyroelectrohydrodynamic force, and then it behaves as a ‘dispensing gun’ that blasts droplets periodically until the electric field vanishes¹⁶.

The pyroelectrohydrodynamic ‘dispensing gun’ presents different functionalities. The shooting direction can be changed within a wide solid angle (Fig. 7a) by moving the thermal source (hot tip or laser beam). In fact, the regions with highest electric fields follow the thermal source displacement.

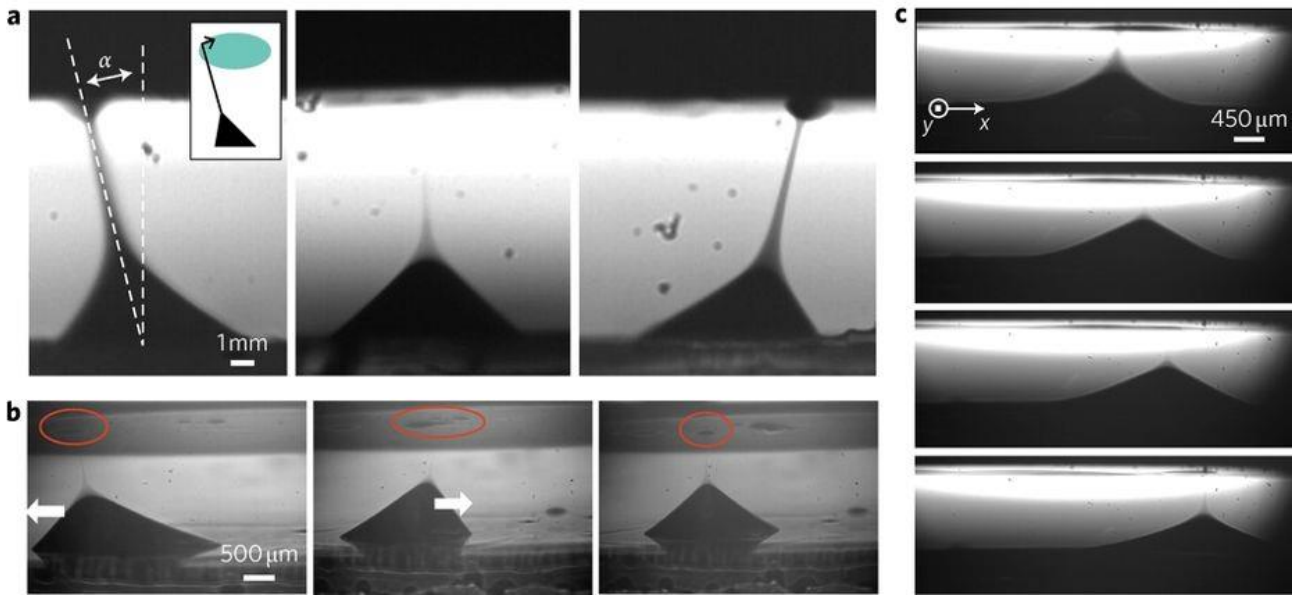


Figure 7 | Functionalities of the dispensing gun.

Larger angles induce the drop reservoir to translate during shooting and dispense to different locations (drop in Fig. 7b and film in Fig. 7c). The drop reservoir moves only beyond a certain threshold angle in fact, when the drop undergoes the maximum asymmetrical deformation under the off-axis electric force, the solid-liquid surface tensions are no longer balanced and a resulting force moves the drop (Fig. 7b). The dispensing gun moves more easily in the case of the film reservoir (Fig. 7c), because no solid-liquid interface tension prevents movement of the blasting cone.

The shooting function can also be synchronized harmonically with the displacement of the droplets while they are dispensed continuously. Such droplets could be collected and managed into a microfluidic system. This function is implemented by positioning the hot tip closer to the edge of the LN plate where the thermal dissipation, favoured by the contact with the glass spacer, generates colder regions¹⁶.

1.2.4 Dispenser improvement

These results show the possibility of drawing and dispensing liquid samples from a drop or film reservoir onto a functionalized substrate such as LN, with intriguing functionalities. However, the deposition of droplets directly onto the warm LN wafer causes spreading of the liquid due to the

electrowetting effect caused by the uncompensated charges generated pyroelectrically on the crystal surface. Moreover, the deposition of droplets onto chips other than the LN plate is desirable so the pyroelectrohydrodynamic dispenser was therefore improved according to the scheme presented in Fig.8:

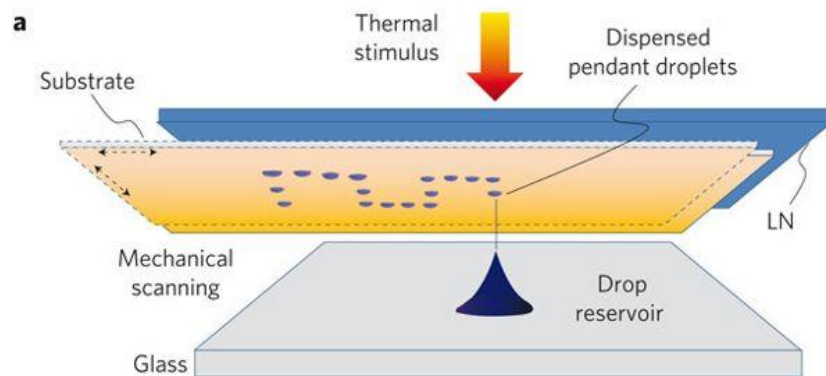


Figure 8 | Improved set-up.

There are three macro-systems composing that setup: a heating system, a moving stage system and a monitoring system. The heating source, which can be a non-contact infrared beam or a hot tip of conventional soldering iron, is in contact with an auxiliary plate of LN wafer. The liquid reservoir is arranged on a glass substrate in front of a second glass substrate, representing the receiver-substrate mounted onto a three axes translation stage, in contact with the LN crystal and on the same line of the heating source. The moving stage system is made up of a high precision linear motor, with an X-Y axis and a digital motion controller. The monitoring system consists of a highly-sensitive and fast camera, an optical zoom lens and a blue LED light source. This last system is used in order to monitor the cone-jet mode and jetting status¹⁶.

This new configuration allows the dispensing gun to be able to print different liquid patterns consisting of separate droplets (with different distances and periods), continuous lines by controlling the translation direction and speed of the substrate and liquid droplets and lines with

highly regular diameters and widths and according to a wide variety of geometries. In the following figure are reported some examples:

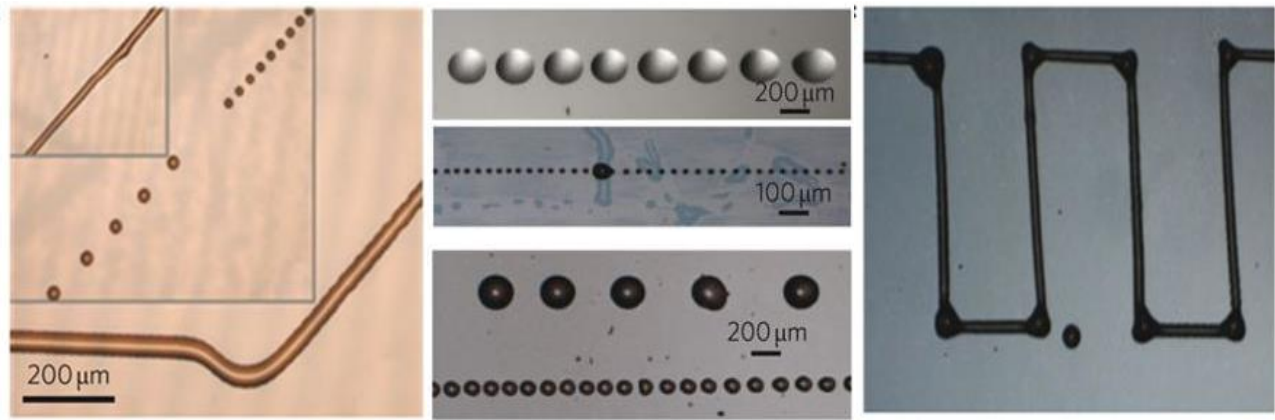


Figure 9| Geometries printed by improved set-up.

The printing process has another intriguing functionality consisting in the simultaneous streaming of adjacent drop reservoirs with different volumes by the same thermal stimulus. A sort of multi-dispensing process is obtained that leads to the formation of parallel lines of droplets of two different diameters.

The major limitation of this configuration was the restriction of the distance between the droplet and the LN crystal: liquid reservoir could not be so far from the crystal, inducing a consequent limitation on thicknesses and geometric constrain of the receiving substrate.

1.2.5 Forward pyro-electrohydrodynamic printing

The problem of the distance is exceeded in a novel configuration proposed: the novelty consists in the placement of the receiving substrate in front of the drop reservoir and of the crystal²².

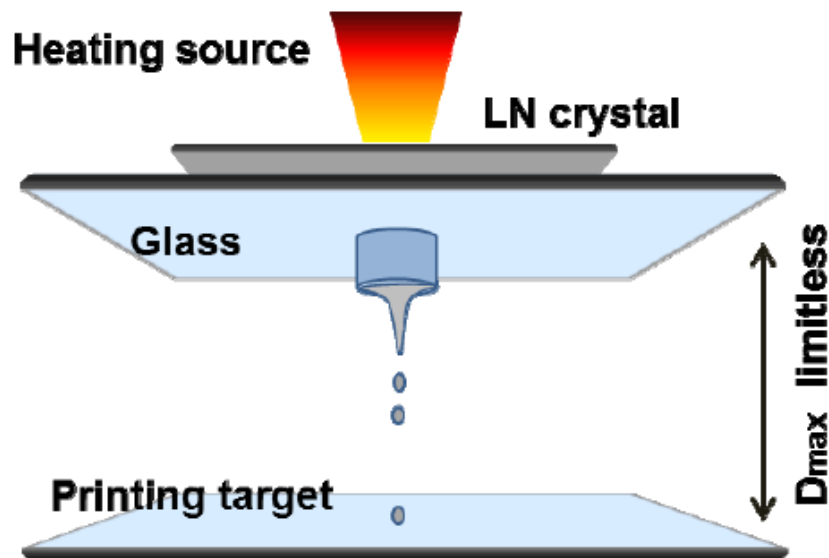


Figure 10| Forward pyro-electrohydrodynamic printing.

This method for direct printing of viscous polymers based on a pyro-electrohydrodynamic repulsion system is capable of overcoming limitations on the material type, geometry and thickness of the receiving substrate.

The new configuration is characterized by the placement of the liquid reservoir that is now in contact or in proximity of the LN. The receiver-substrate is in front of the liquid reservoir and the LN crystal. The liquid drop is mounted onto a polymeric base, previously realized, in order to improve the uniformity of the drop. This base is in contact with a glass substrate. The LN crystal is locally heated, in particular in the area where the placed liquid drop is in contact with the crystal. Once the field is activated, it polarizes the fluid, exerting a repulsive force on the drop and, when it is strong enough, deforms the liquid into a conical tip (Taylor's cone). The drop releases micro-droplets, used for direct printing onto the moving substrate.

The great advantage of this technique consists in the possibility of direct writing micro-drops onto a device, used as the receiving-substrate. In fact, pyro-EHD printing allows to realize high resolution samples, keeping good precision during the printing process, fine spatial resolution onto a very large could be obtained. Moreover, several kinds of inks could be used through pyro-EHD printing.

CHAPTER 2

DROPLET DYNAMICS THROUGH AN ORIFICE

Generally when a droplet interacts with an orifice, it must displace a second fluid and this interaction can be characterized with some parameters such as droplet inertia, gravity, capillary forces, viscous forces, droplet velocity, solid surface properties, solid opening size, wettability, orifice-to-droplet diameter ratio (d/D) and the plate thickness²³. In order to understand how the droplet behaves, a study is necessary.

2.1 Acting forces

If the inertia is sufficient to overcome the surface tension, the droplet can go through the orifice and this interaction can be characterized with the Weber number²⁴, $W_e = \rho_d U_t^2 D / \sigma$, where ρ_d is the droplet density, U_t the approach velocity, D the droplet diameter and σ the surface tension.

In gravity-driven flows the surface tension at the opening orifice acts against the gravity and the interaction can be evaluated with the Bond number²⁵, $B_0 = \Delta\rho g D^2 / \sigma$, in which $\Delta\rho$ is the difference between the droplet density and the surrounding density and g is the acceleration due to the gravity.

After impact the gravitational force that drives the droplet downward can be evaluated as $F_g = \Delta\rho g D^3$ and a characteristic time scale can be defined

$t_g = \sqrt{\frac{\rho_d D}{\Delta\rho g}}$. Depending on the orifice diameter, capillary force and viscous force oppose the droplet motion and two other characteristic times can be

evaluated $t_\sigma = \sqrt{\frac{\rho_d d^3}{\sigma}}$ and $t_\mu = \frac{\rho_d d^2}{\mu_d}$, respectively, for capillary and viscous forces.

In addition, there are two dimensionless numbers, that give information about the prevalent force $R = \frac{t_g}{t_\sigma}$ and the Ohnesorge number²⁶ $Oh = \frac{t_\sigma}{t_\mu}$.

2.2 Droplet and surface properties

Depending on the droplet initial velocity and surface properties, different regimes can occur (Fig.10). In case of hydrophobic hole there are three cases: NI, nonimpregnation regime if the droplet velocity is low; LI, limited impregnation regime if the droplet has an intermediate velocity and SF, slug formation regime, i.e. the formation of a slug that disconnects from the upper part of the liquid, if the velocity is high. For a hydrophilic hole, if the droplet has low velocity it can wets the surface and pass through the hole, so a TI, total impregnation regime occurs; if the droplet has an intermediate velocity there is an air bubble formation between the droplet, B bubbling regime and, if the initial droplet velocity is high a SF regime occurs²⁷.

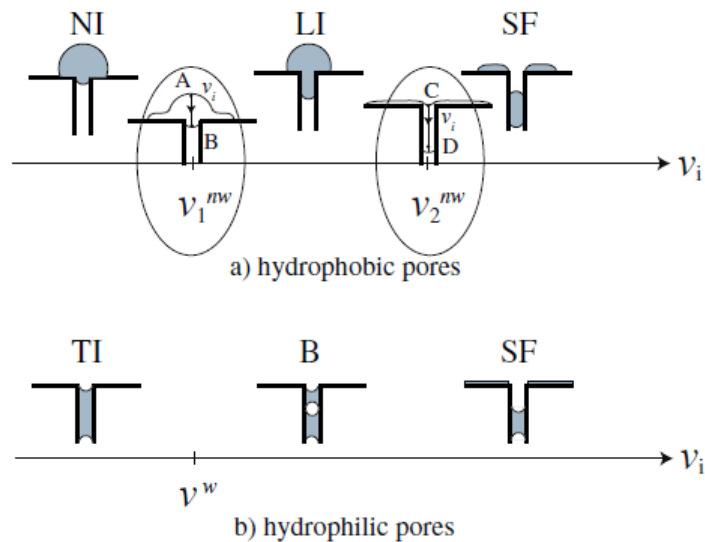


Figure 11|Sketch of the different regimes.

Surface wettability²⁸ is another parameter that can affect the droplet dynamics. With the decrease of contact angle $\theta = 2 \arctg\left(\frac{2H}{D}\right)$, the

droplet is more easily captured, and there exists a critical equilibrium contact angle θ^{eq} when the Bond number and the orifice-to-droplet diameter ratio as well as the thickness of the plate are specified. For the case with $\theta > \theta^{eq}$, the droplet can finally pass through the orifice, otherwise, the droplet cannot pass through the orifice²⁹.

After impact the droplet can either be captured above the surface or it can pass the orifice. This behaviour can be normalized with the t_g . Results from

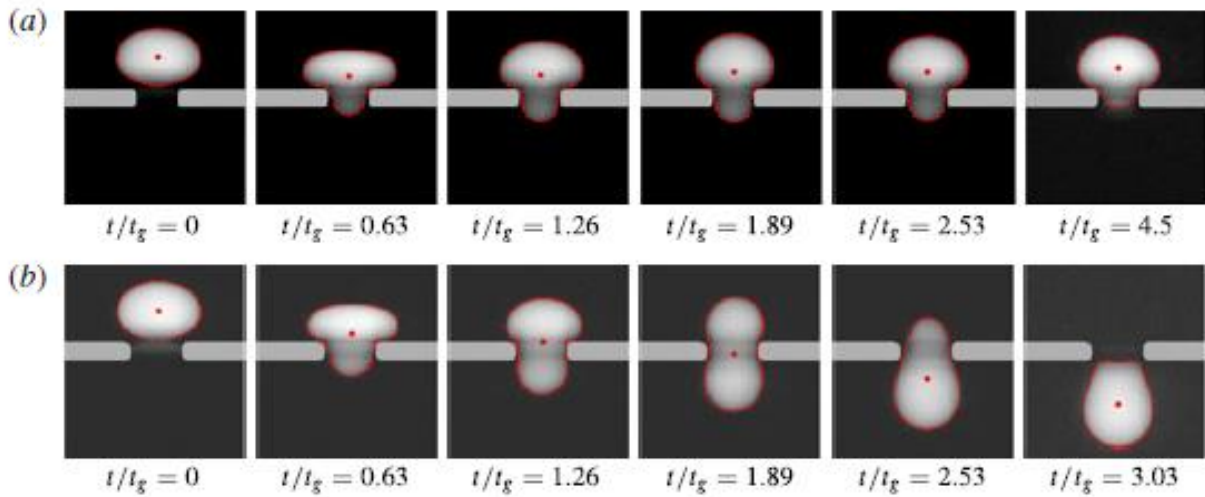


Figure 12| Time sequence of a drop.

the literature observable in Fig.11 show that for a droplet of water/glycerin in a tank filled with silicon oil, for the smaller orifice with $d/D = 0.54$, the maximum asymmetrical deformation occurs at $t=1.26t_g$, after which the droplet retracts backward. When d/D increases, the droplet deformation is smaller and, after $t=1.26t_g$, the lateral interface retraction leads to further penetration of the drop fluid into and through the orifice²³.

Then, regarding the plate thickness, if the thickness is high, the hole behaves as capillary. Results obtained from a droplet of water/ glycerin in a tank filled with silicon oil at fixed contact angles, Bond number and orifice-to-droplet diameter ratio, shows that for a thickness of 8mm the droplet can pass the hole and go out, instead, for a plate thickness of 1.2mm the drop is not able to pass the hole²⁹.

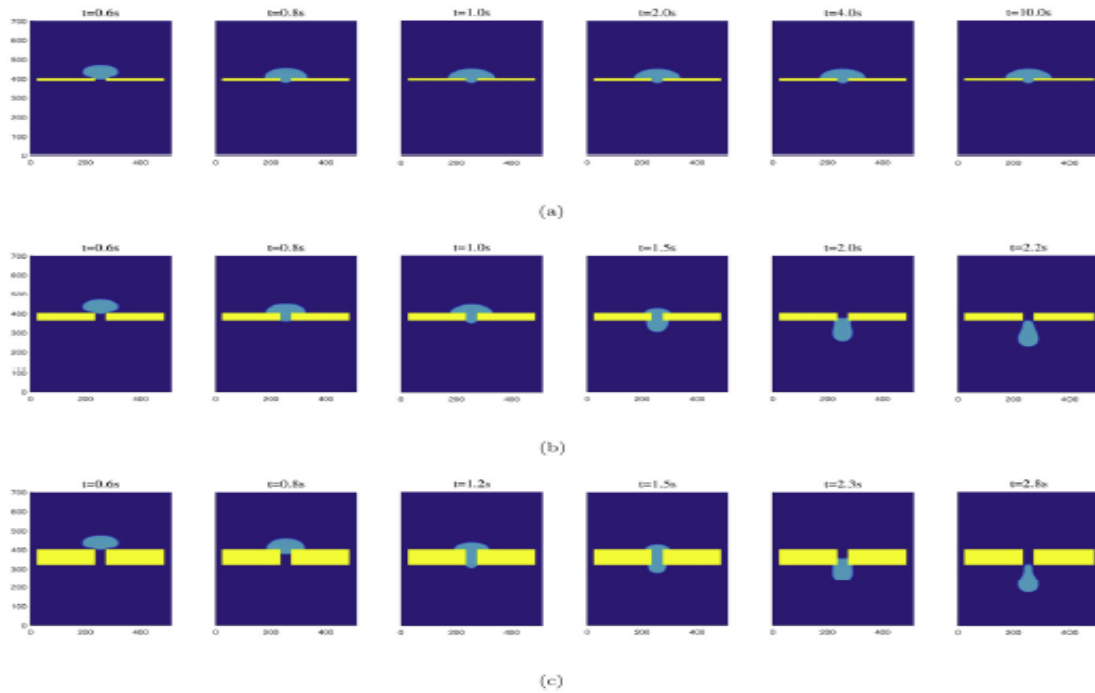


Figure 13| Droplet through an orifice.

CHAPTER 3

MATERIALS AND METHODS

Numerical simulations, firstly, and experimental test, subsequently, have been performed in order to determine the characteristics of the orifice geometry and to study the dynamics of a droplet exiting from an orifice.

3.1 Simulations

The process of drop impact is generally difficult to simulate because of its highly transient nature. The length scales the thin free sheets and thin wall films produced by drop impact are often several orders smaller than the initial drop diameter.

Therefore, a reliable simulation of the drop impact phenomena requires an extremely fine numerical mesh. The geometry and a fine numerical mesh (Fig.14) have been defined in COMSOL Multiphysics by adopting an axisymmetric³⁰ geometry as reported in Fig. 14:

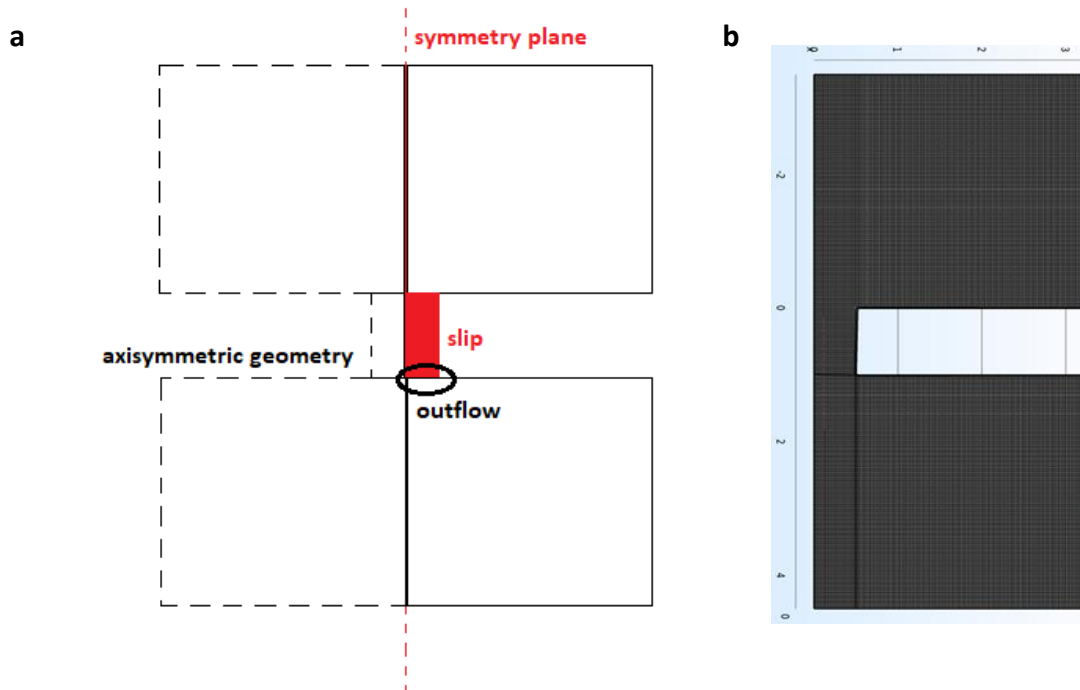


Figure 14| Axisymmetric geometry and mesh. a Representation of axisymmetric geometry with boundary conditions and **b** mesh generated by COMSOL Multiphysics.

The physics of this phenomenon suggests that there are several competitive effects influencing the flow field during impact and the final outcome after the impact: gravity, viscous, inertial and surface tension forces.

Therefore, to study meniscus formation and air-water interface, simulations were done in OpenFOAM.

OpenFOAM (Open Field Operation And Manipulation) is a C++ toolbox for the development of customized numerical solvers, and pre-/post-processing utilities for the solution of continuum mechanics problems, most prominently including computational fluid dynamics (CFD).

To study droplet meniscus formation and air-water interface, Volume-Of-Fluid (VOF) simulations were done in OpenFOAM.

In VOF method the transport equation (1) for the volume fraction of one phase is solved simultaneously with the continuity (2) and momentum equations (3):

$$\frac{\partial \alpha}{\partial t} + \nabla \cdot (\mathbf{U}\alpha) = 0 \quad (1)$$

$$\nabla \cdot \mathbf{U} = 0 \quad (2)$$

$$\frac{\partial(\rho \mathbf{U})}{\partial t} + \nabla \cdot (\rho \mathbf{U} \mathbf{U}) = -\nabla p + \nabla \cdot \mathbf{T} + \rho \mathbf{f}_b \quad (3)$$

where \mathbf{U} represents the velocity field shared by the two fluids throughout the flow domain, α is the phase fraction, \mathbf{T} is the deviatoric viscous stress tensor $\{\mathbf{T}=2\mu\mathbf{S}-2\mu(\nabla \cdot \mathbf{U})\mathbf{I}/3$ with the mean rate of strain tensor $\mathbf{S}=0.5[\nabla \mathbf{U}+(\nabla \mathbf{U})^T]$, and $\mathbf{I} \equiv \delta_{ij}$, ρ is density, p is pressure, and \mathbf{f}_b are body forces per unit mass (gravity and surface tension effects at the interface)³¹. In VOF simulations the latter forces include gravity and surface tension effects at the interface. A relevant parameter is the phase fraction α that can take values ranging from 0 to 1 ($0 \leq \alpha \leq 1$), where 0 and 1 correspond to regions accommodating only one phase, e.g., $\alpha=0$ for gas and $\alpha=1$ for liquid. Accordingly, gradients of the phase fraction are encountered only in the region of the interface.

In order to solve differential equations, the software needs some boundary conditions (see Fig. 14) such as:

- outflow on the outlet boundaries;
- axial symmetry on the axis of symmetry;
- slip with a prescribed contact angle on the walls.

Two immiscible fluids are considered as one effective fluid throughout the domain, the physical properties of which are calculated as weighted averages based on the distribution of the liquid volume fraction, thus being equal to the properties of each fluid in their corresponding occupied regions and varying only across the interface,

$$\rho = \rho_l \gamma + \rho_g (1 - \gamma) \quad (4)$$

$$\mu = \mu_l \gamma + \mu_g (1 - \gamma) \quad (5)$$

in which ρ_l and ρ_g are the densities of liquid and gas phase.

One of the critical issues in numerical simulations of free surface flows using the VOF model is the conservation of the phase fraction. This is especially the case in flows with high density ratios, where small errors in volume fraction may lead to significant errors in calculations of physical properties. Accurate calculation of the phase fraction distribution is crucial for a proper evaluation of surface curvature, which is required for the determination of surface tension force and the corresponding pressure gradient across the free surface. The interface region between two phases is typically smeared over a few grid cells and is therefore highly sensitive to grid resolution.

VOF simulations have been made on a water [13] droplet initially spherical (or equivalently ellipsoidal) with different initial radius (or major and minor axes) in an air domain. The physical parameters for the two phases necessary to solve the problem are reported in Tab.1:

PHISYCAL PARAMETERS (WATER/AIR SYSTEM)	
Droplet Viscosity	0.001 Pa*s
Droplet Density	1000 Kg/m ³
Surface tension	0.07 N/m
Contact Angle	60° ⁽¹⁾
Air Density	1 Kg/m ³
Air Viscosity	1,48* 10 ⁻⁵ m ² /s

Table 1 | Physical parameter of water/air system.

Also, the start/stop times and the time step for the run must be set.

The run starts at t=0. For end time setting it is requested to reach the steady state solution where the flow is circulating around the cavity, so a value around 0.15 has been demonstrated to be sufficient. At last,

¹ Value obtained with hesaglas sample provided by VUB.

timestep option specifies that results are written every n th time step where the value n is specified under the writeInterval keyword. Time values utilized in this study are reported in Tab. 2:

startTime	0
endTime	0.15
writeInterval	0.001

Table 2| Time intervals for simulations.

At the end, ParaView has been utilized for visualizing data.

3.2 SensApp set-up

The pyro-electrohydrodynamic-jet (p-jet) is a radically innovative method that uses the pyroelectric effect to produce tiny droplets (down to about 10-6pL). A pyroelectric slab is able to generate a charge density on the surface when subjected to a transient and slight temperature (T) gradient. The resulting electric field causes the ejection of tiny droplets from the mother drop. The p-jet draws daughter droplets directly from the meniscus of the mother drop pipetted by the operator on the loading support (e.g. 2 μ L), producing the smallest volumes.

A schematic set-up configuration, called “top-down”, is reported in Fig. 15:

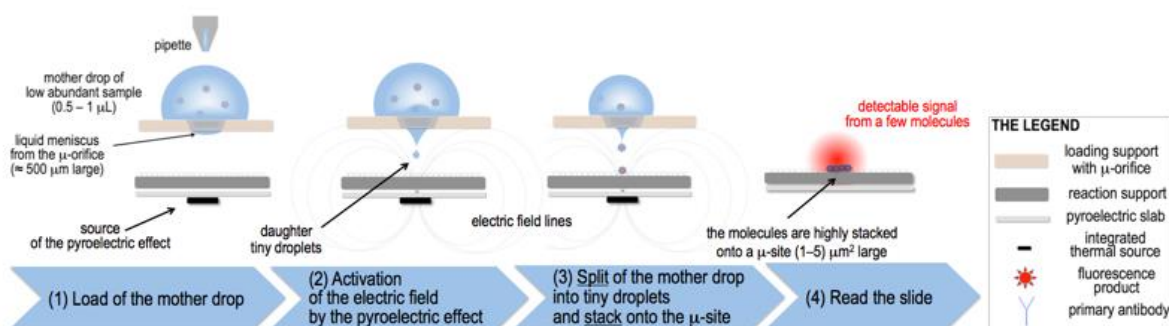


Figure 15| Set-up configuration.

It is possible to observe that a mother drop of sample is loaded on the engineered μ -orifice of the loading support to form a thin liquid meniscus on the opposite face. A slab (reaction support) is functionalized by immobilizing the appropriate antibody (high density and high affinity with the antigen in sample), and faces the μ -orifice. A pyroelectric slab, functionalized by a point-wise thermal source aligned with the μ -orifice, works as source of the pyro-electrohydrodynamic jet (p-jet) that triggers the rapid dispensing of tiny daughter droplets onto the same site (' μ -site') of the reaction support. For simplicity, the antigen molecules in Fig.15 are fluorescent but, in reality, they are labelled by secondary reactions after stacking.

Actual set-up of pyro-electrohydrodynamic system is similar to that reported in Fig. 10 with the μ -heater in the opposite position.

As reported in Fig. 16, it is constituted by a μ -heater realized in Tungsten, a LN slide, a receiver amino substrate, and a loading support made by a polymer, such as PMMA with the μ -orifice.

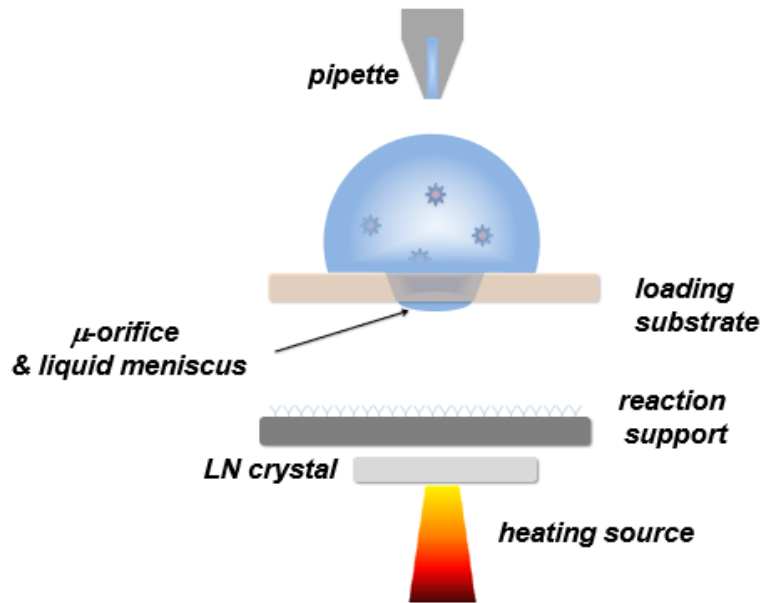


Figure 16 | Actual set-up of Pyro-EHD system.

The amino substrate is used in order to make the immuno-reactions happen. It is a commercial slide, produced by Arrayit Corporation, used to immobilize biomolecules in order to make microarrays.

3.2.1 Heat transfer devices

In order to generate the pyroelectric effect, it is necessary to apply a temperature gradient on LN slide. According to First Joule Law $P=V \cdot I$, an electrical circuit has been used with the aim to obtain a thermal power. μ -heater (see Figure 17) has been fabricated in lab workshop with a Tungsten wire having $300\mu\text{m}$ diameter. The final shape is dictated by the need to have a pointed stimulus.



Figure 17 | μ -heater. Top and side picture of μ -heater.

The electrical circuit is set by enabling the power supply (Lab. Grade Switching Mode Power Supply HCS-3300 in Fig.17) and a waveform generator (33220A Function / Arbitrary Waveform Generator, 20 MHz see Fig.17) is utilized to set a unit step function with assigned on and off times.



Figure 18| Power supply and waveform generator.

The choice of a unit step function is governed by the necessity to have a predefined period in which the current passage is assured/enabled, and another period without current in order to activate and deactivate the μ -heater with a fixed time lapse. The input function is a discontinuous function with zero values for negative arguments, corresponding to absence of current in the μ -heater and one for positive arguments, matching the current passage.

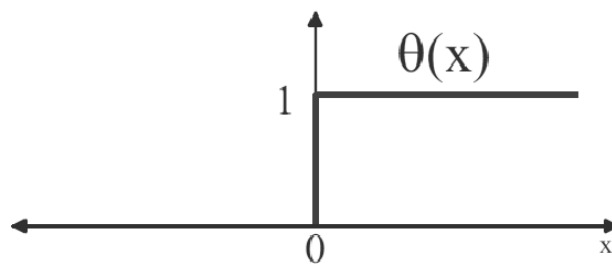


Figure 19|The unit step function.

Then a fan cooler is positioned in the bottom part of the set-up.

CHAPTER 4

RESULTS

The aim of this chapter is to report the results of simulations and experimental results starting from which it has been possible to give geometric characteristic to the device. Then based on these results, other tests have been performed in order to refine the set-up with the purpose to observe droplets formation.

4.1 Device geometry

Steady-state simulations have been performed by replacing the droplet dynamics in order to observe the thickness of drop meniscus and set the geometric parameters.

The general scheme for geometry is reported in Fig. 20, then, with a fixed contact angle (θ) of 60° , changes/variations have been applied to:

- channel radius;
- channel height;
- channel inclination angle;
- orifice and upper substrate wettability.

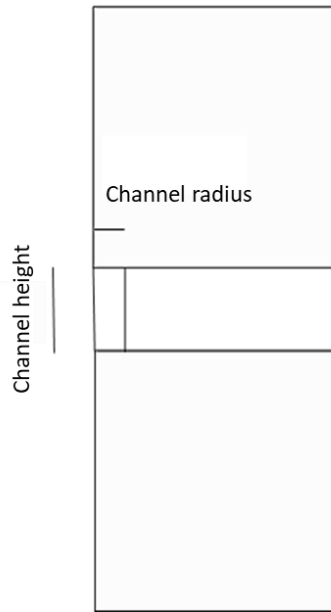


Figure 20| Input geometry.

A summary of the simultaneous variables' changes applied to the initial geometry is reported in Tab.3:

Channel inclination angle α [°]	Channel height H [mm]	Channel radius R [mm]	Droplet radius R [mm]
1	1	[0.25; 0.5; 1]	[1; 1.5; 2; 2.5]
	1.5	0.5	[1; 1.5; 2]
5	1	0.5	[1; 1.5; 2; 2.5]
	1.5	0.5	[1; 1.5; 2]
10	1	0.5	[1; 1.5; 2; 2.5]
	1.5	0.5	[1; 1.5; 2]
20	1	0.5	[1; 1.5; 2; 2.5]
	1.5	0.5	[1; 1.5; 2]
30	1	0.5	[1; 1.5; 2; 2.5]
	1.5	0.5	[1; 1.5; 2]
40	1	0.5	[1; 1.5; 2; 2.5]
	1.5	0.5	[1; 1.5; 2]

Table 3| Simulations parameters.

4.1.1 Droplet meniscus shape as a function of the geometry

First of all, in order to set the initial droplet shape, two simulations have been done, respectively, with a spherical and an ellipsoidal drop having the same initial volume passing through a channel with radius 0,5mm and height 1mm.

In the following figure, on left is reported the spherical case and on right the droplet with ellipsoidal initial shape; upper images represent the initial instant ($t=0$) and in the bottom images are reported final instants once a steady-state is attained.

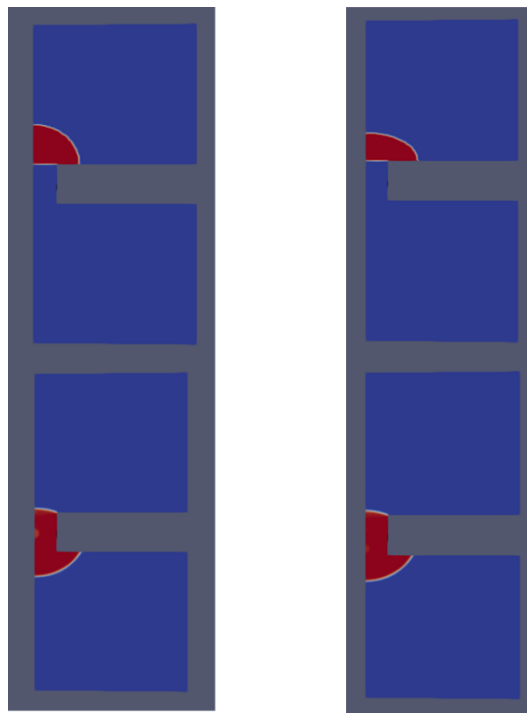


Figure 21 | Meniscus of spherical and ellipsoidal droplets.

The results reported in Fig.21 show that the meniscus shape is the same so this suggests that is equivalent to simulate a spherical or an ellipsoidal initial droplet.

After that, in order to provide a visual feedback of the Tab.3, some simulations results have been reported by fixing the channel radius and height and varying the inclination angle for two droplet radii:

- Firstly, the effect of inclination angles variation has been tested on a geometry with characteristics reported in Tab.4:

Inclination Channel [°]	Channel radius [mm]	Channel height [mm]
1	0,5	1
5		
10		
20		
30		
40		

Table 4

For:

1. Droplet radius 1mm

$\alpha=1^\circ$ $\alpha=5^\circ$ $\alpha=10^\circ$ $\alpha=20^\circ$ $\alpha=30^\circ$ $\alpha=40^\circ$

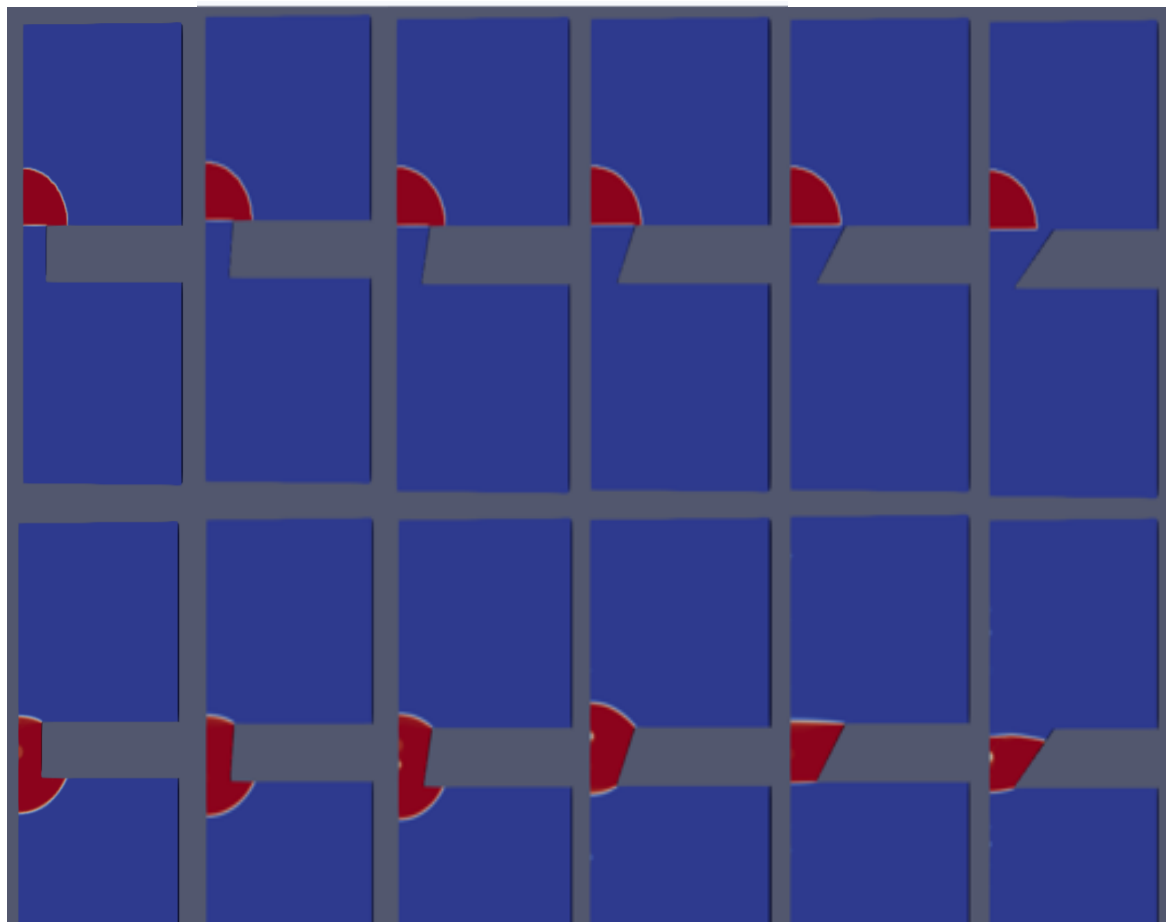


Figure 22 | Droplet radius 1mm. Initial (up) and final (down) snapshots, respectively, for drop dynamic through a channel with $r=0,5\text{mm}$, $h=1\text{mm}$ and an increasing α .

Acceptable menisci are the last three cases since the droplet does not become larger than the orifice dimension.

2. Droplet radius 2mm

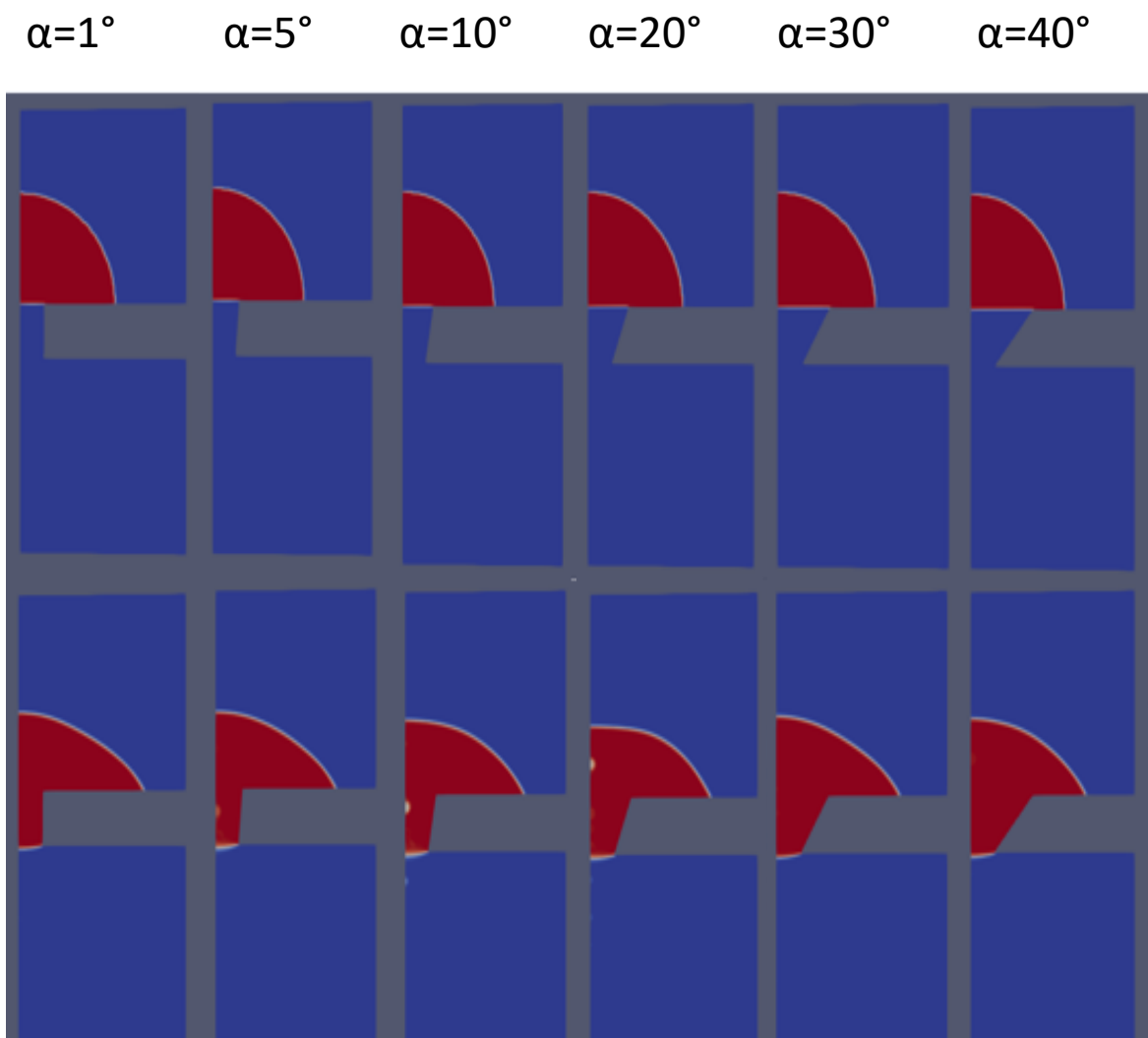


Figure 23 | Droplet radius 2mm. Initial(up) and final(down) snapshots, respectively for a drop dynamic through a channel with $r=0,5\text{mm}$, $h=1\text{mm}$ and an increasing α .

When droplet has an initial radius of 2mm, based only on a visual observation, it could be said that all the channel inclination angles are able to generate an acceptable meniscus shape.

➤ Changes have been imported to geometry:

Inclination Channel [°]	Channel radius [mm]	Channel height [mm]
1	1	1
5		
10		
20		
30		
40		

1. Droplet radius 1mm

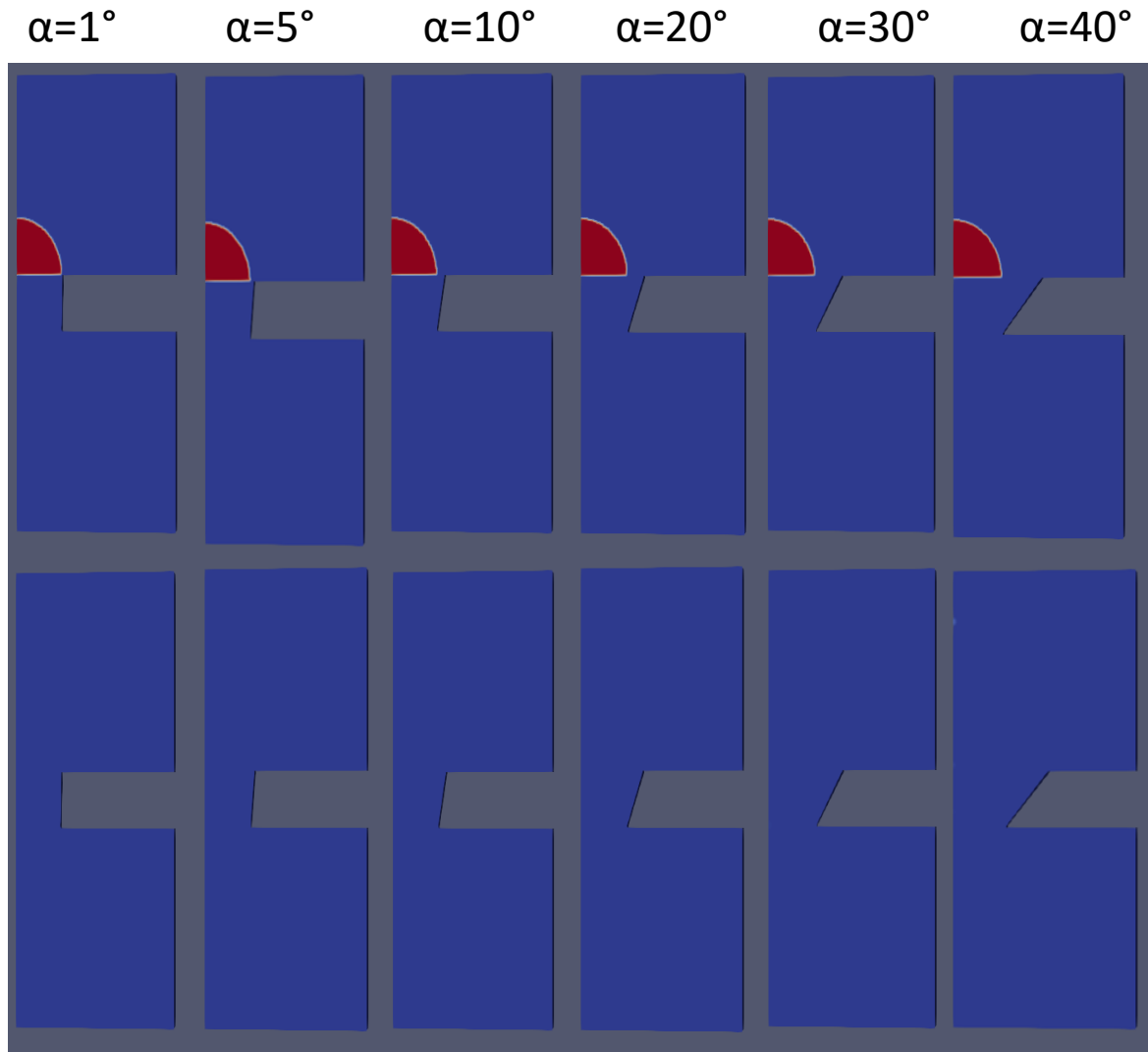


Figure 24| Droplet radius 1mm. Initial(up) and final(down) snapshots, respectively for a drop dynamic through a channel with $r=1\text{mm}$, $h=1\text{mm}$ and an increasing α .

In the case in which the channel radius has the same dimension of the droplet radius, since the channel is subjected to an inclination, it happens that the upper orifice radius is bigger than the droplet so the droplet goes down through the channel without the need to set on the electric field.

2. Droplet radius 2mm

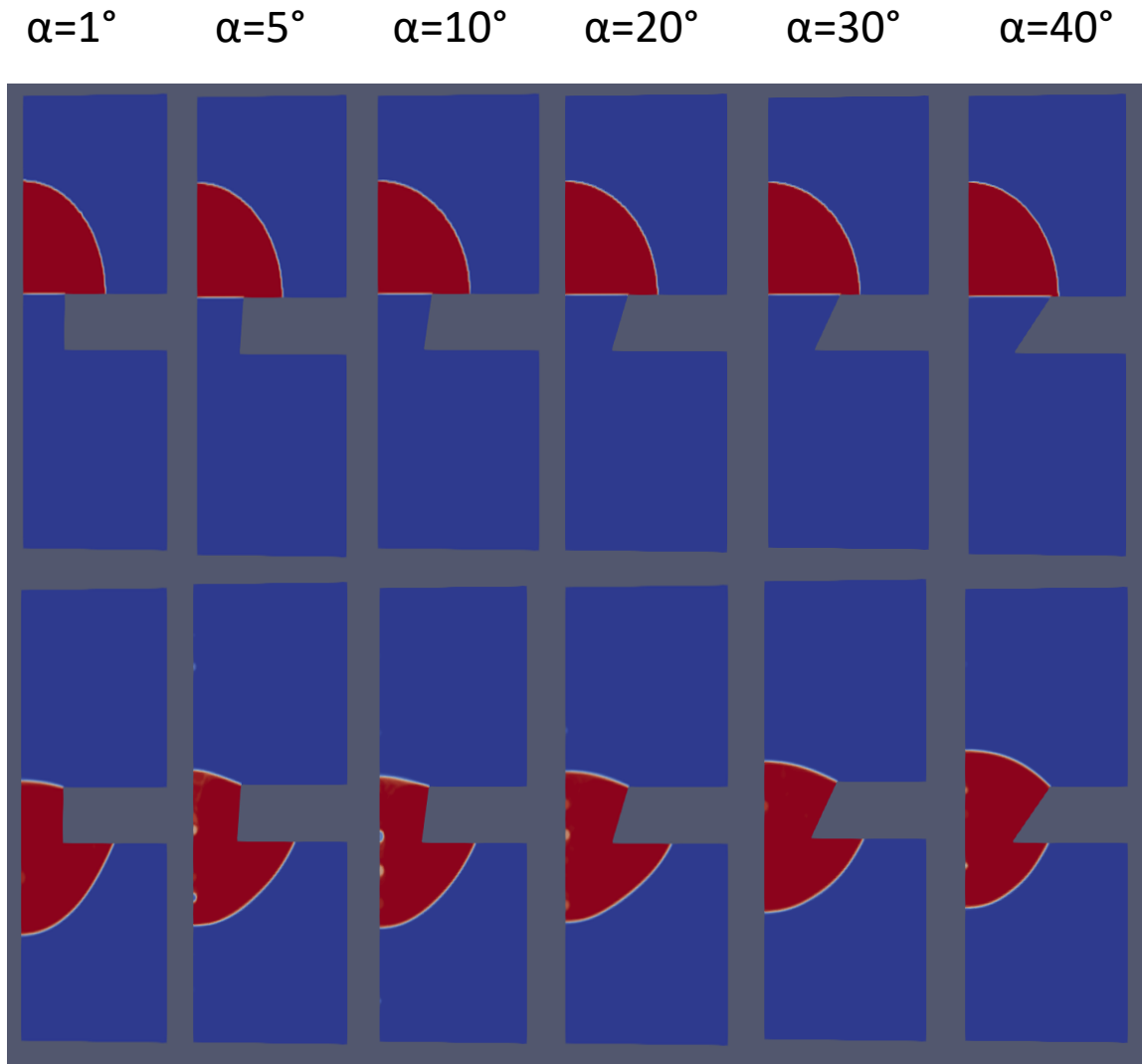


Figure 25 | Droplet radius 2mm. Initial(up) and final(down) snapshots, respectively for a drop dynamic through a channel with $r=1\text{mm}$, $h=1\text{mm}$ and an increasing α .

A different situation happens when the initial droplet radius is 2mm, so bigger than the orifice radius. In this case, whatever the channel inclination is, the droplet goes through the channel and exhibits a meniscus too big, so this case cannot be useful.

- Then, by changing the geometry other investigations have been made:

Inclination Channel [°]	Channel radius [mm]	Channel height [mm]
1	0.5	1.5
5		
10		
20		
30		
40		

1. Droplet radius 1mm

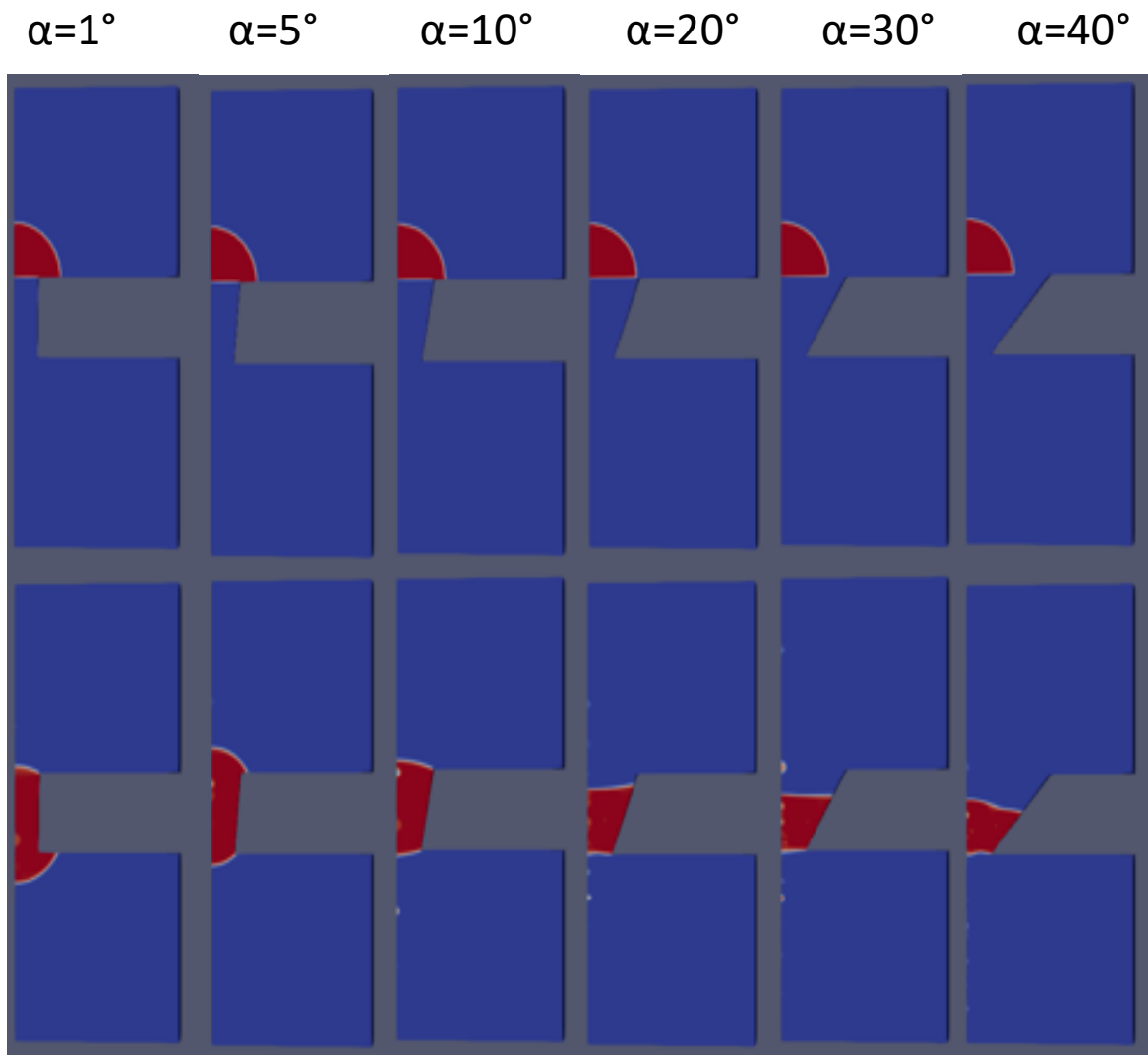


Figure 26 | Droplet radius 1mm. Initial(up) and final(down) snapshots, respectively for a drop dynamic through a channel with $r=0.5\text{mm}$, $h=1.5\text{mm}$ and an increasing α .

When the channel is stretched but with small radius, the channel inclination angle is a critical parameter.

In this case just α equal to 10° and 30° is able to provide a right meniscus shape.

2. Droplet radius 2mm

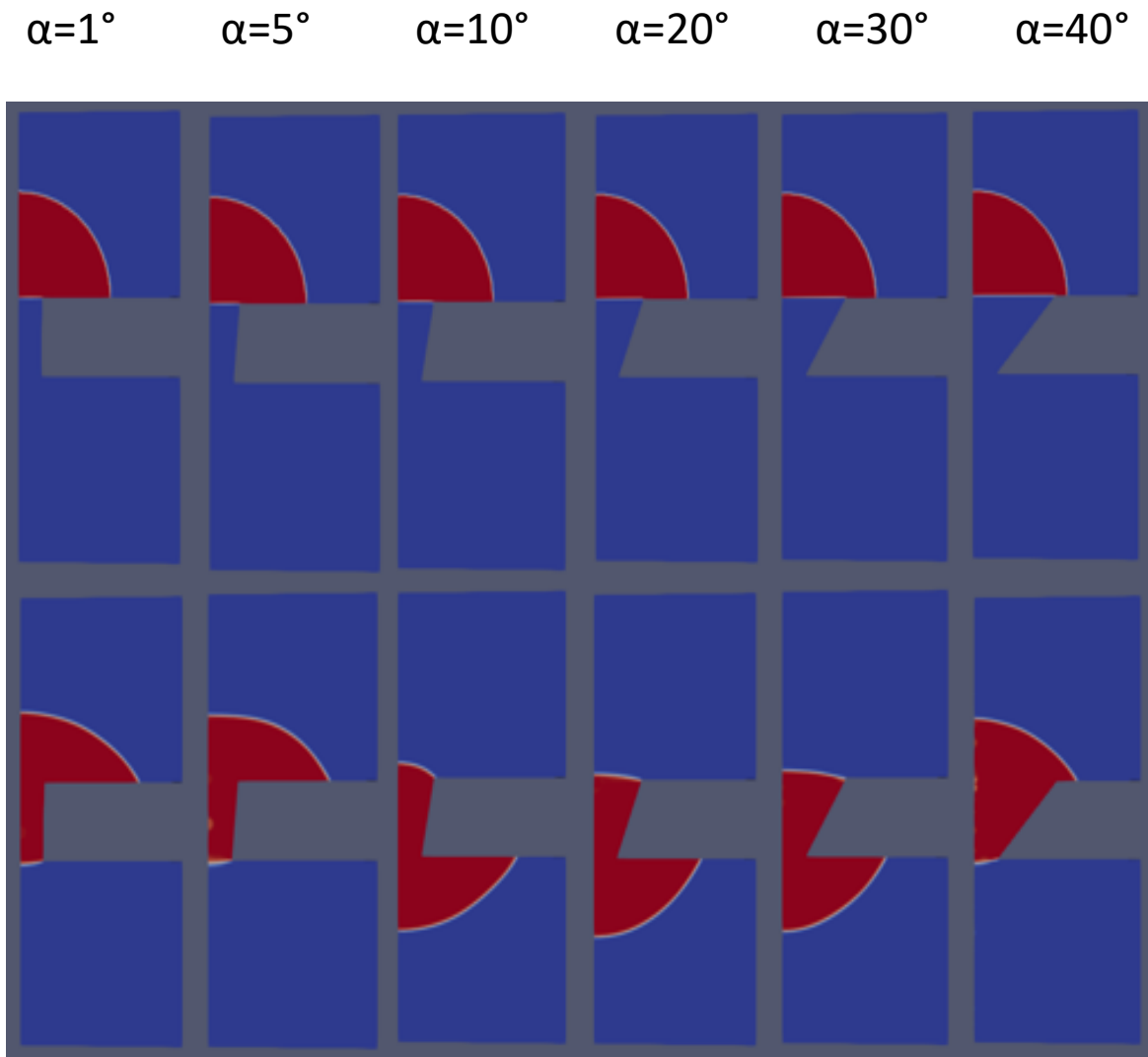


Figure 27| Droplet radius 2mm. Initial(up) and final(down) snapshots, respectively for a drop dynamic through a channel with $r=0,5\text{mm}$, $h=1,5\text{mm}$ and an increasing α .

By increasing the droplet radius, more interesting situations can be observed. In this condition significant menisci shapes could be observed when α assumes values of 1° , 5° and 40° .

A measure of the meniscus thickness is necessary to establish which are the best/right geometric characteristics. These estimations have been made with ImageJ program by measuring T segment reported in Fig.28:

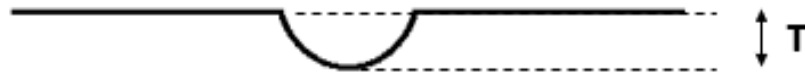


Figure 28| Meniscus thickness.

Hence different menisci have been selected to make meniscus thickness measurement.

- i. Channel dimensions: $\left\{ \begin{array}{l} \text{radius} = 0.5\text{mm} \\ \text{height} = 1\text{mm} \end{array} \right.$

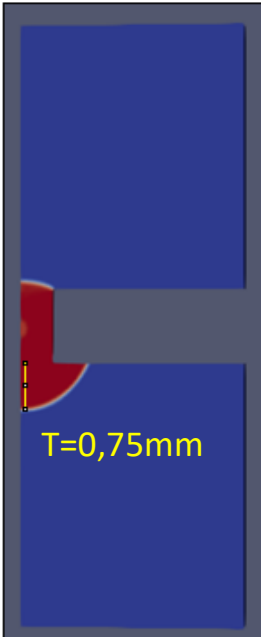

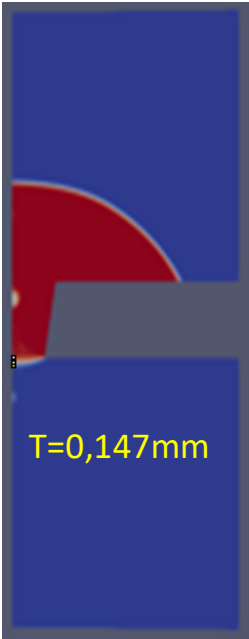
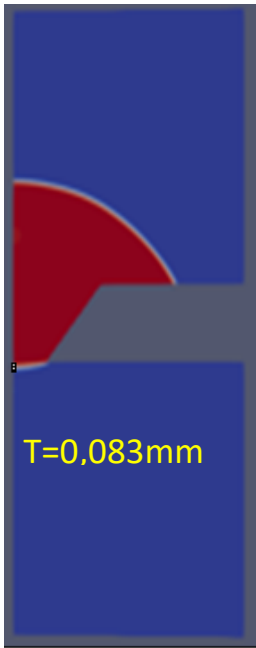
Droplet radius 1mm		Droplet radius 2mm	
$\alpha = 1^\circ$	$\alpha = 40^\circ$	$\alpha = 1^\circ$	$\alpha = 40^\circ$
			

Table 5| Menisci thickness. Menisci thickness measurements for channel radius 0.5mm and channel height 1mm.

- ii. Channel dimensions: $\left\{ \begin{array}{l} \text{radius} = 1\text{mm} \\ \text{height} = 1\text{mm} \end{array} \right.$

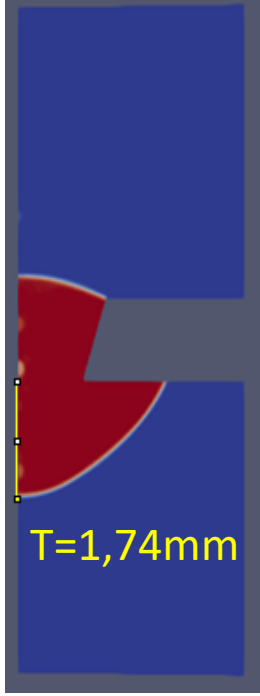
Droplet radius 1mm	Droplet radius 2mm
$\forall \alpha$ value	$\alpha = 20^\circ$
No meniscus thickness measurement because droplet exits from the orifice	 <p>T=1,74mm</p>

Table 6| Meniscus thickness. Meniscus thickness measurement for channel radius 1mm and channel height 1mm.

- iii. Channel dimensions: $\left\{ \begin{array}{l} \text{radius} = 0.5\text{mm} \\ \text{Height} = 1.5\text{mm} \end{array} \right.$

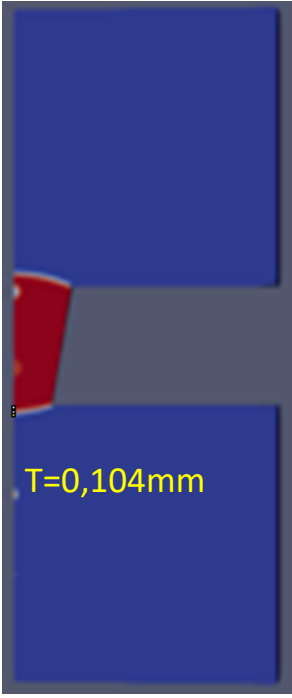
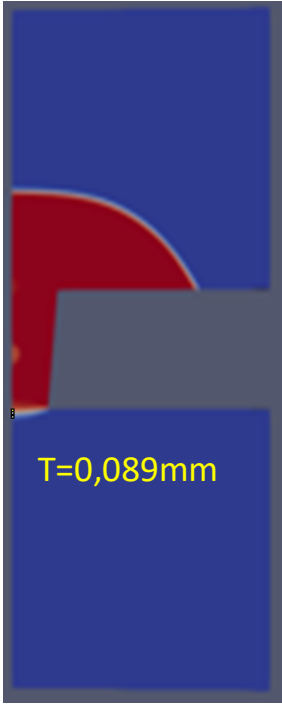
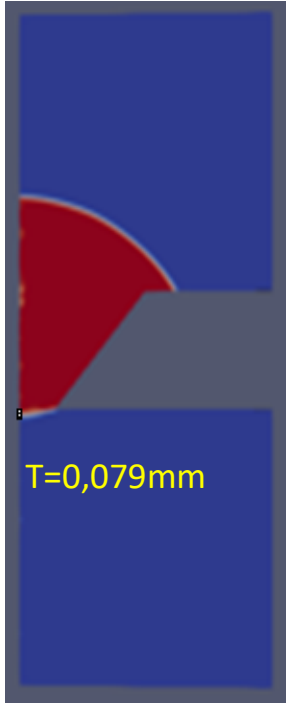
Droplet radius 1mm	Droplet radius 2mm	
$\alpha = 10^\circ$	$\alpha = 5^\circ$	$\alpha = 40^\circ$
		

Table 7| Menisci thickness. Menisci thickness measurements for channel radius 0.5mm and channel height 1.5mm.

Since SensApp objective is the detection of small volume droplet, a meniscus thickness around 100 μm is the desired condition.

Based on this assumption and desiring to start with as small as possible droplet volume (that means small droplet radius), it can be concluded that the best meniscus thickness measure has been obtained in case of a droplet with 1mm radius goes through a channel with radius 0.5mm, height 1mm and inclination angle 40° .

Therefore, considering simulations results, the fabrication of a PMMA slide with an orifice having 0.3mm radius and inclination angle about 40° has been requested to VUB partner.

4.1.2 P-jet test in orifice

Droplet behavior through 0.3 mm radius, 2mm height and $\alpha 47^\circ$ (real value of VUB orifice) orifice has been investigated firstly with numerical simulations, then with experimental study under pyroelectric field.

The dynamics of the droplet, the shape of the meniscus and the formation of daughter droplets are analysed.

4.1.2.1 Simulation results

In this section data analysed with ParaView are reported.

The following figure 29 shows the simulation results for the mother drop with radius 2.6mm (the dimension of the droplet has been set in order to avoid it is smaller than the upper orifice radius). The upper row shows the initial condition, whereas the bottom row refers to the final configuration once the meniscus is equilibrated (even if the steady state has not yet been reached).



Figure 29| Droplet radius 2.6mm. Initial(up) and intermediate(down) snapshots, respectively for a drop dynamic through a channel with $r=0,3\text{mm}$, $h=2\text{mm}$ and $\alpha=47^\circ$.

As said before, in red is represented the water phase and in blue the gas phase, while the interfaces show an intermediate colour. Then, concerning the meniscus, the desired thickness about 100 μm is obtained.

4.1.2.2 Laboratory tests

Liquid dispensing from the orifice in a plastic plate (PMMA) under pyroelectric field is the first and foremost task of SensApp. Hereby, the results of experimental study of the liquid droplet within the orifices made by VUB group with pyroelectric field applied are summarized.

Using a loading support with μ -orifice large 0.3 mm radius furnished by VUB group, various kinds of samples with different surfactants have been investigated and they are reported below in Table 4:

SAMPLES				
		β -amyloid concentration [=] $\mu\text{g/ml}$	Labels	
1	β -Amyloid in distilled water		50	β -Amy
2	β -Amyloid solution	&Triton 0,04%	50	β -Amy/Triton
3	β -Amyloid solution	&Tween 0,04%	50	β -Amy/Tween Low
4	β -Amyloid solution	&Tween 10%	50	β -Amy/Tween High
5	β -Amyloid solution	& Glycerol 10%	50	β -Amy/Glycerol
6	β -Amyloid & DMSO 1% solution		50	β -Amy/DMSO

Table 8|Samples. Samples analysed under p-jet.

The following figure shows the experimental results for cases listed above:

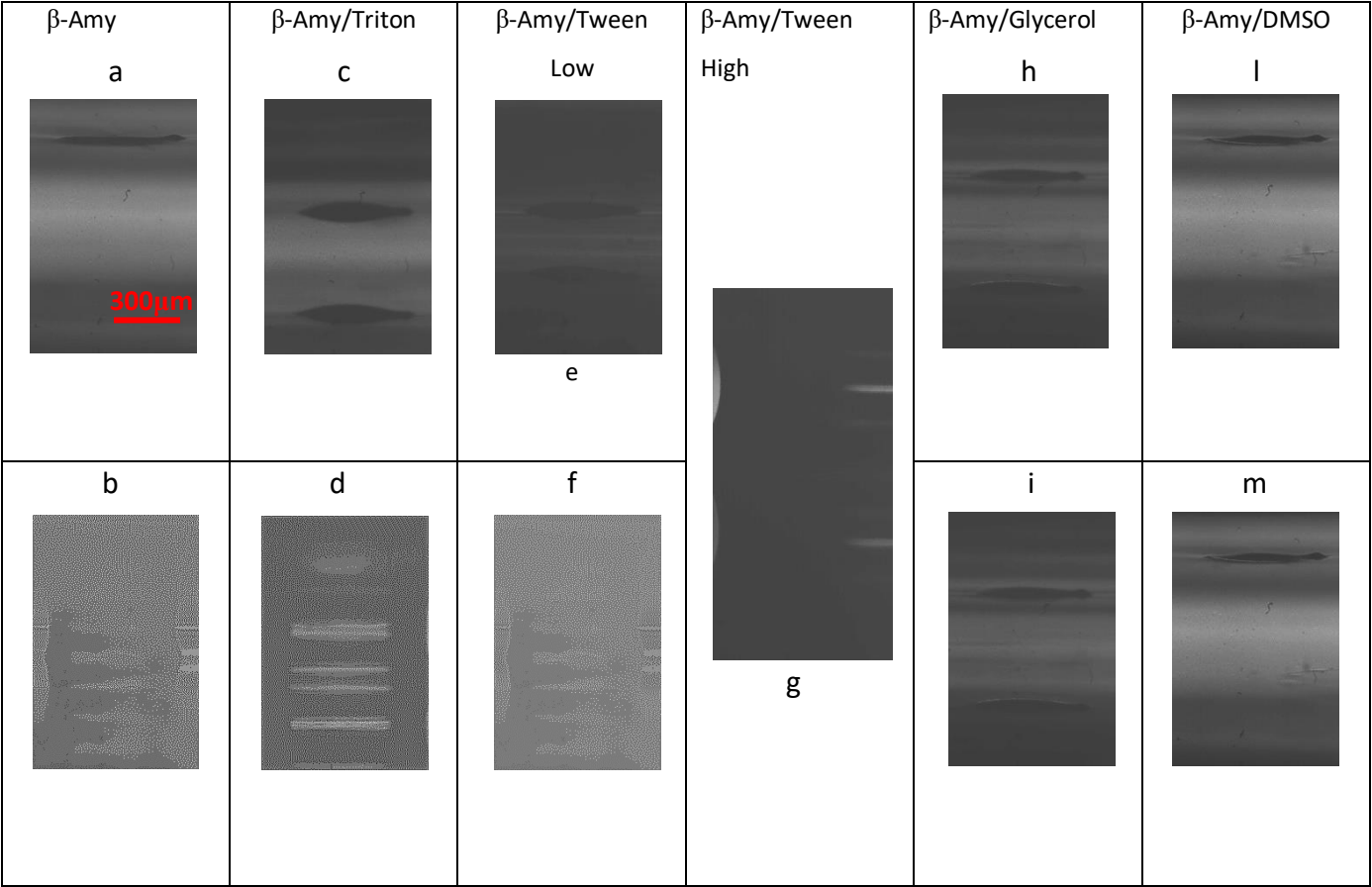


Figure 30| Experimental results. Initial and final snapshots of the experiments results.

❖ β -Amyloid in distilled water experiments have been performed two times obtaining different results:

1. No effect of the electric filed on the mother drop;
2. Stable liquid bridge;

3. β -Amyloid & Triton 0,04% solution under the application of an electric field responses with a stable liquid bridge;
4. β -Amyloid & Tween 0,04% solution under the application of an electric field responses with a stable liquid bridge;
5. β -Amyloid & Tween 10% solution behaves in a different way it spontaneously empties the reservoir before the application of the electric field;
6. β -Amyloid & Glycerol 10% solution, no effect of the electric field can be appreciated on the mother drop;
7. β -Amyloid & DMSO 1% solution, no effect of the electric field can be appreciated on the mother drop.

The meniscus morphology obtained in the simulation shown in figure 29 appears in good agreement with the experimental results shown in figure 30 a. A measurement has been done with ImageJ; in both cases meniscus thickness is $\sim 35\mu\text{m}$.

The bridge formation under the electric field action appears to be strictly related to the meniscus thickness: thicker meniscus produces larger bridges.

In conclusion, it is possible to say that the numerical simulations help to understand the droplet dynamics exiting from an orifice.

The physics of this phenomenon dictates that there are several competitive effects influencing the flow field: gravity, viscous, inertial and surface tension forces. As expected, dealing with capillary tube, the surface tension is the prevalent force.

To support this thesis the relationship between the gravity force and the surface tension has been defined by evaluating the Bond Number²⁵ :

$$Bo = \frac{\Delta\rho g D^2}{\sigma}$$

where $\Delta\rho = \rho_d - \rho_s$ is the difference between the droplet and the surrounding densities; g is the gravity acceleration; D is the droplet diameter and σ is the surface tension.

Since investigated samples can be considered as similar as water (see Report on Viscosity Measurements, Eng. Simona Itri), an analysis on water droplet positioned on 0.3mm orifice radius surrounded by air has been performed with the following data:

$$\sigma = 0,07 \frac{kg}{s^2} \quad g = 9,81 \frac{m}{s^2} \quad \rho_d = 1000 \frac{kg}{m^3} \quad \rho_s = 1 \frac{kg}{m^3}$$

$$\Delta\rho = 999 \frac{kg}{m^3}$$

By considering an initial droplet volume of 2 μ L, droplet diameter can be estimated:

$$V_d = \frac{4}{3}\pi r^3$$

$$r = \sqrt[3]{\frac{3 V_d}{4\pi}} = 0,78mm \rightarrow D = 1,56mm$$

Hence the Bo number can be evaluated:

$$Bo = \frac{\Delta\rho g D^2}{\sigma} = 0,34$$

It means that $F_g = 0,34\sigma$, so the surface tension is the prevalent force ($\sigma > F_g$).

Therefore, numerical predictions and experimental simulations are an optimal tool to analyse dynamics of a droplet exiting from an orifice.

According to the main results discussed in this report and those previously obtained by home-made orifices (see Report on home-made orifices, Volodymyr Tkachenko (Researcher CNR)), it can be concluded that it is not necessary proceed with larger VUB orifice (diameters equal to 1.02, 1.0, 0.88 mm) but with those one having smaller dimensions (diameters equal to 0.4, 0.3, 0.2 and 0.1 mm).

In conclusion it can be said that the formed volume exiting from the orifice has the dimensions/diameter of the orifice. Therefore, based on this consideration, since SensApp long-term goal is highly sensitive detection of low abundant molecules and since this investigation leads to observe that there is bridge formation, incoherent with concentrated droplets, it can be concluded that, in order to obtain a pointed meniscus, two ways can be adopted:

- smaller orifice;
- microarray pin.

The first solution is currently work in progress by VUB partner; the second alternative has been investigated, as usual, with simulations and laboratory tests.

4.2 Droplet formation

The choice to resort to a device including microarray printing pin has been dictated by the necessity to have a pointed meniscus and by considering that the charge density growing at a smaller radius of curvature, so a commercial solution with microarray pin has been tested.

Conventional use of printing pin is characterized by a contact between pin and substrate, instead this innovative technique overtakes this method exploiting p-EHD effect.

Therefore, a microarray pin with a capillary channel provided by VTT partner and fabricated by Arrayit has been used.

4.2.1 Printing pin geometry

A picture of pin and the relatively geometry are reported in Fig.31:

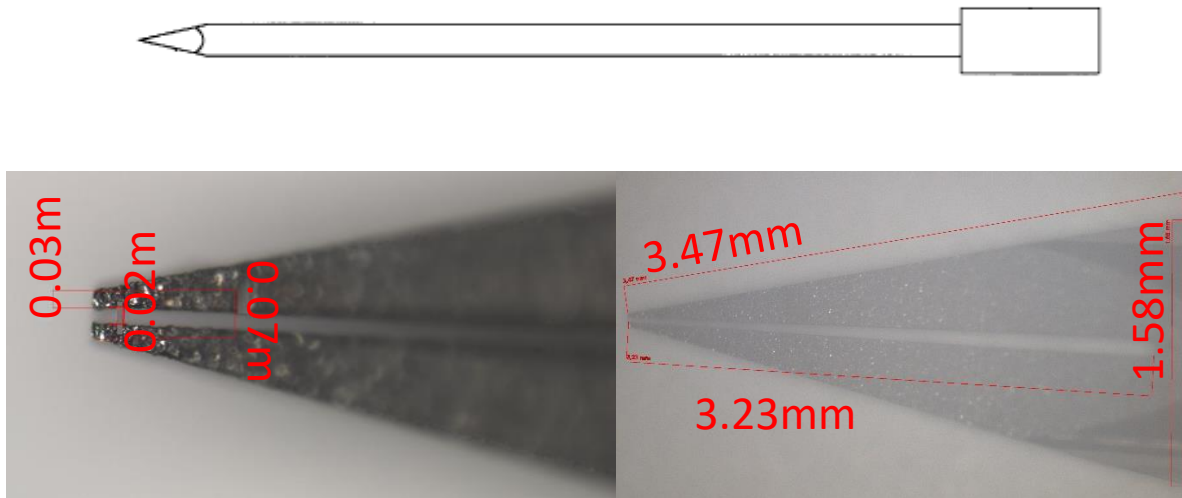


Figure 31| Printing pin.

It is constituted by two parts: the shaft, made out of 440-C stainless steel, and the collar, made out of 303 stainless steel³².

Dimensions measurements have been obtained by acquiring images with Zeiss microscopy.

4.2.2 Simulations

Simulations of droplet dynamics through the orifice in which a pin is positioned have been made with a different geometry having 0.5 mm channel radius, 0.3 mm channel height and by varying the initial pin position.

Since nowadays OpenFOAM simulations are performed without the electric field application, for sake of simplicity the presence of channel in pin is neglected.

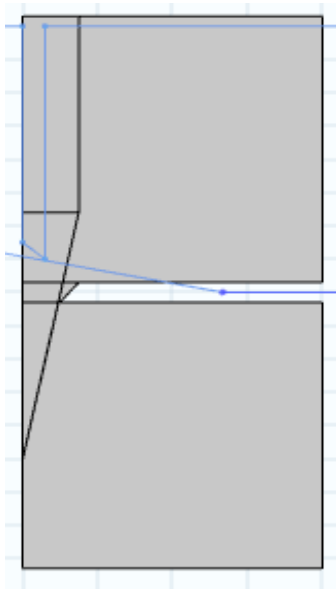


Figure 32 | Geometry with pin.

In order to generate an extremely fine mesh in COMSOL Multiphysics pin surface has been subtracted to the entire geometry as reported in Fig.33:

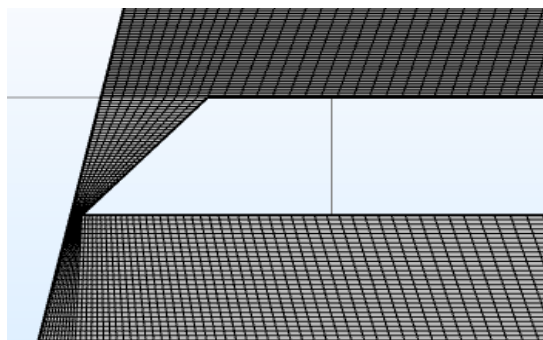


Figure 33 | Mesh for geometry with printing pin.

Simulations have been made on a water droplet with the characteristics as reported in Tab.1 but with different value of contact angle. In the current situation two contact angles must be considered:

- contact angle water/pin=60°;
- contact angle water/substrate=77°.



Figure 36| Simulation output.

Simulation output performed on pin crossing the channel shows that water droplet is not able to reach tip pin. This suggests that the pin needs to stay over so that only the final part of the tip cross goes through the channel.

4.2.3 Experimental tests

Laboratory tests have been performed in order to understand if the presence of printing pin in the orifice is able to change droplet dynamics under electric field.

Printing pin reported in Fig.31 has been mounted in the orifice after sample loading.

4.2.3.1 Voltage and step function settings

A preliminary investigation about the voltage value needed to have droplet dispensing together with the necessity to avoid Tungsten incandescence has been performed, followed by an investigation on time interval for current passage in Tungsten μ -heater necessary to have receiving substrate temperature between 25°C and 36°C (critical temperature value to avoid protein degradation).

In order to perform such tests, an initial voltage value and time interval have been set, then Tungsten incandescence and droplets jetting have been observed.

To set the time interval, a step function like that reported in Fig.30 has been utilized, where “ON time” represents time lapse in which current passes

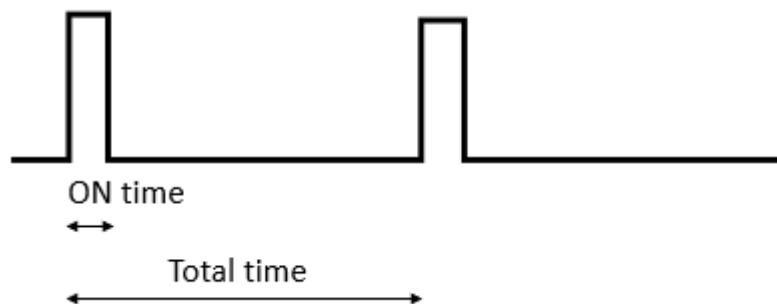


Figure 35| Step function. Total time and ON time representation.

through the Tungsten wire, “total time” is the time interval of each event and “OFF time” = total time – ON time is the time lapse between each current stimulus.

In the following table tests results are schematized:

Voltage [V]	ON time [s]	OFF time [s]	Total time [s]	Incandescence	Droplet formation
2.4	3.0	57.0	60	✓	✓
	1.5	58.5		✓	X
2.2	3.0	57.0	60	✓	✓
2.0	5.0	55.0	60	✓	✓
	3.5	56.5		✓	✓
	3.0	57.0		✓	X
1.6	3.5	56.5	60	X	✓
1.5	4.0	56.0	60	X	✓
	3.5	56.5		X	✓

Table 9| Laboratory materials setting.

Results summarized in Tab.8 suggest that the optimal conditions to have droplets formation without μ -heater incandescence by using set-up with printing pin are:

Voltage [V]	ON time [s]	OFF time [s]	Total time [s]
1.6	3.5	56.5	60

4.2.3.2 Laboratory results

By adopting voltage and time intervals values demonstrated optimal in the previous analysis, laboratory tests with printing pin have been performed. The observed phenomenon can be summarized as shown in Fig.36:

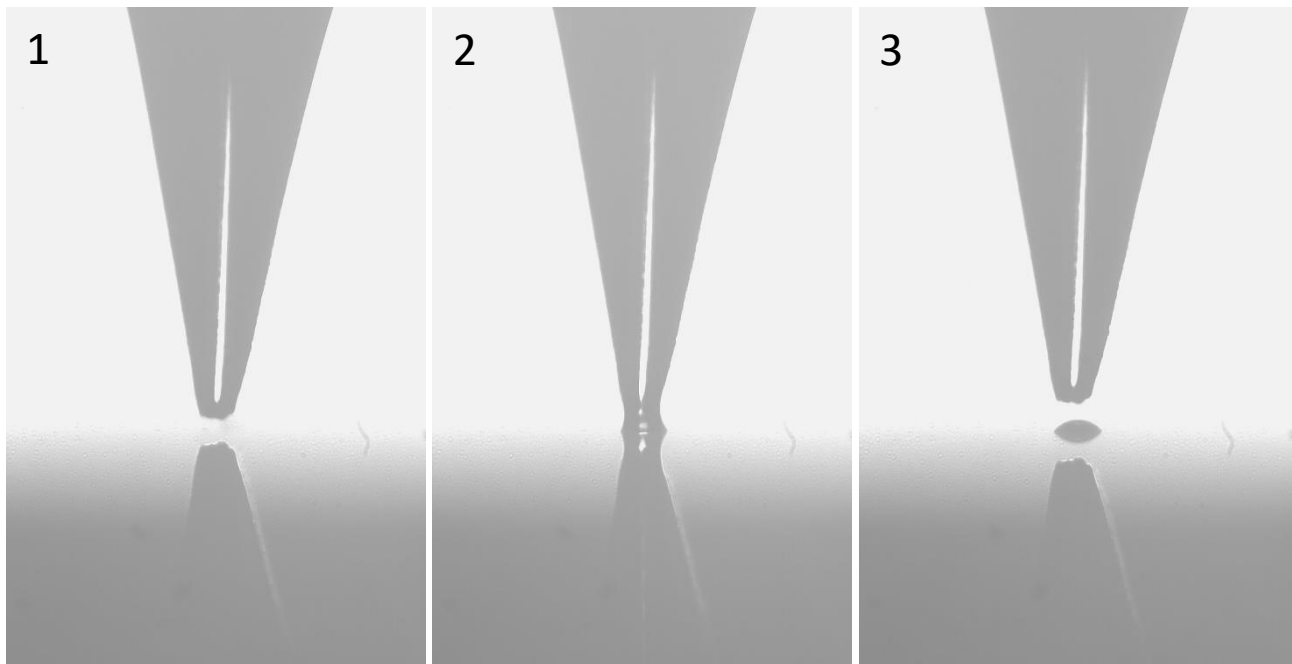


Figure 36| Droplet deposition by pyro-electro-hydrodynamic jetting.

Three images have been selected representing three times instants:

- 1) Initial instant: just the cable pin is observable;
- 2) Droplet deposition instant: the phenomenon of droplet deposition occurs;
- 3) Droplet deposited: on the substrate deposited droplet can be seen.

This configuration has allowed to carry out experiments by making twenty jets (which means twenty droplets deposition) for each pointed site.

Two samples with different β -Amyloid concentrations (500pg/mL and 50ng/mL) in distilled water have been analysed.

Subsequently acquisition from Fluorescence Scanner has been performed in order to study the signal intensity. In figure 37 are reported the

Fluorescence Scanner output, in which the columns represent the two samples and the rows are the repeated experiments for each sample.

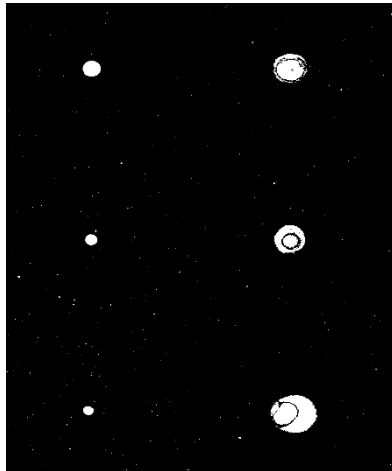


Figure 37| Fluorescence Scanner output.

As showed in figure 37 samples printed with printing pin by applying pyro-electro-hydrodynamic effect is able to produce an interesting and important signal.

4.2.4 Wettability tests

Last investigation is about the influence of orifice wettability on the droplet dynamics.

In order to do this, two contact angles (θ) values between water and orifice substrate have been simulated:

- $\theta=77^\circ$;
- $\theta=15^\circ$.

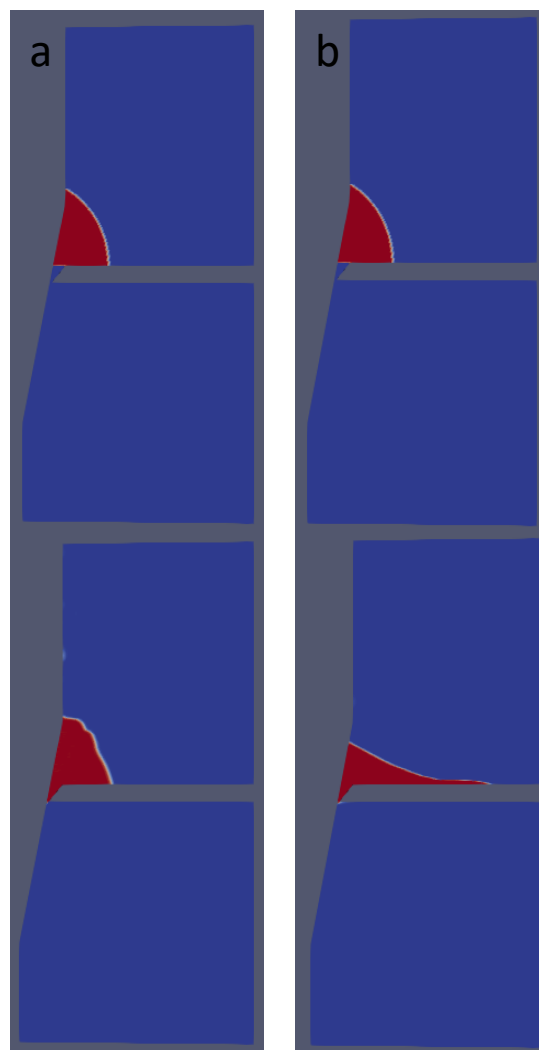


Figure 37| Simulations output. Output of simulations with **a** contact angle 77° and **b** contact angle 15° .

This analysis was useful to affirm that with the aim to have a pointed meniscus, so the formation of droplets with small volumes, is necessary to use a starting substrate (equivalently an orifice) with a contact angle about 70° .

CHAPTER 5

CONSLUSIONS AND PERSPECTIVES

Actual set-up, showed in Fig.13, derives from the need to build a device for routine analysis that allows the operator to easily load the sample.

SensApp goal is the jet of droplets with small volumes, so a protruding meniscus exiting from the orifice is needed.

Studies performed with Software simulations and experimental tests on an orifice with 0.3mm radius and 47° inclination angle show that the results are in agreement, but the bridge connecting the two substrates is not the required situation, since it is not coherent with the desired concentrated droplets.

Therefore, in order to obtain a pointed meniscus, two ways have been proposed: small orifices or the integration of printing pin in the orifice. The first solution is a work in progress alternative, instead the other one has been tested and it has given promising results.

In conclusion an optimal jetting effect was observed in tests with the printing pin and droplet with the same tip pin dimensions (around 25µm) have been printed.

The main purpose of this thesis work has been to demonstrate that simulations are a good tool to predict the droplet dynamics through the orifice since all simulations results are in agree with laboratory tests results.

Nowadays the entire protocol with immuno-reactions have been performed by using solutions having β -Amyloid concentration till 500 pg/ml. Signal analysis done with Fluorescence Scanner showed interesting results, so the next step is to go down till 1 pg/ml β -amyloid concentration.

Regarding the mathematical simulation aspect, future investigations could be performed by introducing electric field in OpenFOAM simulations.

References

1. Clark, M. F., Lister, R. M. & Bar-Joseph, M. ELISA techniques. in *Methods in Enzymology* vol. 118 742–766 (Academic Press, 1986).
2. SensApp. *SensApp* <http://www.sensapp.eu/>.
3. Wang, H., Chen, L. & Sun, L. Digital microfluidics: A promising technique for biochemical applications. *Front. Mech. Eng.* **12**, 510–525 (2017).
4. Pan, Y., Huang, Y., bu, N. & Yin, Z. Fabrication of Si-nozzles for parallel mechano-electrospinning direct writing. *J. Phys. Appl. Phys.* **46**, 255301 (2013).
5. Lang, S. B. *Sourcebook of pyroelectricity*. (Gordon and Breach Science Publishers, 1974).
6. Lang, S. B. Pyroelectricity: From Ancient Curiosity to Modern Imaging Tool. *Phys. Today* **58**, 31–36 (2005).
7. Ferroelectric Polymers | Science.
<https://science.sciencemag.org/content/220/4602/1115>.
8. Whatmore, R. W. Pyroelectric devices and materials. *Rep. Prog. Phys.* **49**, 1335–1386 (1986).

9. Thermocouple temperature measurement - Ghent University Library.
<https://lib.ugent.be/catalog/rug01:000763588>.
10. Weis, R. S. & Gaylord, T. K. Lithium niobate: Summary of physical properties and crystal structure. *Appl. Phys. A* **37**, 191–203 (1985).
11. López-Herrera, J., Popinet, S. & Herrada, M. A charge-conservative approach for simulating electrohydrodynamic two-phase flows using Volume-Of-Fluid. *J Comput Phys.* **230**, 1939–1955 (2011).
12. Zeleny, J. Instability of Electrified Liquid Surfaces. *Phys. Rev.* **10**, 1–6 (1917).
13. Disintegration of water drops in an electric field | Proceedings of the Royal Society of London. Series A. Mathematical and Physical Sciences.
<https://royalsocietypublishing.org/doi/10.1098/rspa.1964.0151>.
14. Fujii, O., Honsali, K., Mizuno, Y. & Naito, K. Vibration of a water droplet on a polymeric insulating material subjected to AC voltage stress. *IEEE Trans. Dielectr. Electr. Insul.* **17**, 566–571 (2010).
15. Melcher, J. R. & Taylor, G. I. Electrohydrodynamics: A Review of the Role of Interfacial Shear Stresses. *Annu. Rev. Fluid Mech.* **1**, 111–146 (1969).

16. Ferraro, P., Coppola, S., Grilli, S., Paturzo, M. & Vespini, V. Dispensing nano–pico droplets and liquid patterning by pyroelectrodynamic shooting. *Nat. Nanotechnol.* **5**, 429–435 (2010).
17. Fabrication of polymer lenses and microlens array for lab-on-a-chip devices | (2016) | Olivieri | Publications | Spie.
<https://spie.org/publications/journal/10.1117/1.OE.55.8.081319?SSO=1>.
18. Rosenblum, B., Bräunlich, P. & Carrico, J. P. Thermally stimulated field emission from pyroelectric LiNbO₃. *Appl. Phys. Lett.* **25**, 17–19 (1974).
19. Ahmed, R. & Jones, T. B. Optimized liquid DEP droplet dispensing. *J. Micromechanics Microengineering* **17**, 1052–1058 (2007).
20. Park, J.-U. *et al.* High-resolution electrohydrodynamic jet printing. *Nat. Mater.* **6**, 782–789 (2007).
21. Maeda, N., Israelachvili, J. N. & Kohonen, M. M. Evaporation and instabilities of microscopic capillary bridges. *Proc. Natl. Acad. Sci.* **100**, 803–808 (2003).

22. Coppola, S. *et al.* Direct fabrication of polymer micro-lens array. in *Optical Measurement Systems for Industrial Inspection X* vol. 10329 103294Q (International Society for Optics and Photonics, 2017).
23. Bordoloi, A. D. & Longmire, E. K. Drop motion through a confining orifice. *J. Fluid Mech.* **759**, 520–545 (2014).
24. Weber Number - an overview | ScienceDirect Topics.
<https://www.sciencedirect.com/topics/engineering/weber-number>.
25. Roth, B. The Bond Number. *Medium*
<https://medium.com/@bradroth/the-bond-number-19d489c58f76>
(2019).
26. Ohnesorge Numbers | Practical Coatings Science | Prof Steven Abbott.
<https://www.stevenabbott.co.uk/practical-coatings/ohnesorge.php>.
27. Delbos, A., Lorenceau, E. & Pitois, O. Forced impregnation of a capillary tube with drop impact. *J. Colloid Interface Sci.* **341**, 171–7 (2010).
28. Surface Wettability - an overview | ScienceDirect Topics.
<https://www.sciencedirect.com/topics/engineering/surface-wettability>.

29. Yuan, X. & Shi, B. Dynamic behavior of droplet through a confining orifice: A lattice Boltzmann study. *Comput. Math. Appl.* (2019) doi:10.1016/j.camwa.2018.12.044.
30. Axisymmetric Analysis - A problem in which the geometry, loadings, boundary conditions and materials are symmetric with respect to an axis is one that can be solved as an axisymmetric problem instead of as a three dimensional problem.
http://mae.uta.edu/~lawrence/ansys/thick_cylinder/thick_cylinder.htm#targetText=Axisymmetric%20Analysis%20%2D%20A%20problem%20in%20which%20the%20geometry%2C%20loadings%2C,as%20a%20three%20dimensional%20problem.&targetText=The%20Y%20axis%20is%20the%20axis%20of%20symmetry.
31. Phys. Rev. E 79, 036306 (2009) - Drop impact onto a liquid layer of finite thickness: Dynamics of the cavity evolution.
<https://journals.aps.org/pre/abstract/10.1103/PhysRevE.79.036306>.
32. S, M. R. Microarray Printing Device Including Printing Pins With Flat Tips And Exterior Channel And Method Of Manufacture. (1998).

Previous studies helpful to end up with the actual device set-up are here reported:

[1] S. Grilli et al. Active accumulation of very diluted biomolecules by nano-dispensing for easy detection below the femtomolar range. *Nature communications* 5, 5314

[2] V. Vespini et al. Forward electrohydrodynamic inkjet printing of optical microlenses on microfluidic devices. *Lab on a Chip* 16 (2), 326-333

[5] S. Coppola et al. Self-assembling of multi-jets by pyro-electrohydrodynamic effect for high throughput liquid nanodrops transfer *Lab on a chip* 11 (19), 3294-3298

[6] L. Mecozzi et al. Simple and rapid bioink jet printing for multiscale cell adhesion islands. *Macromolecular bioscience* 17 (3), 1600307

[7] O. Gennari et al. Investigation on cone jetting regimes of liquid droplets subjected to pyroelectric fields induced by laser blasts. *Applied Physics Letters* 106 (5), 054103

[8] L. Mecozzi et al. Easy Printing of High Viscous Microdots by Spontaneous Breakup of Thin Fibres. *ACS applied materials & interfaces*

[9] S. Coppola et al. Nanocomposite polymer carbon-black coating for triggering pyro-electrohydrodynamic inkjet printing. *Applied Physics Letters* 106 (26), 261603

[10] L. Miccio et al. Hemicylindrical and toroidal liquid microlens formed by pyro-electro-wetting. *Optics letters* 34 (7), 1075-1077

[11] L. Mecozzi et al. Spiral formation at the microscale by μ -pyro-electrospinning. *Soft matter* 12 (25), 5542-5550

[12] M. De Angelis et al. Plasmon resonance of gold nanorods for all-optical drawing of liquid droplets. Applied Physics Letters 103 (16), 163112

[13] Report on Viscosity Measurements, Eng. Simona Itri.

[14] Report on home-made orifices, Volodymyr Tkachenko (Researcher CNR).

Acknowledgments

The authors acknowledge the EU funding within the Horizon 2020 Program, under the FET-OPEN Project “SensApp”, Grant Agreement n.829104.

Thanks to Professors Pier Luca Maffettone and Gaetano D’Avino for the immense availability. I’m glad to have shared part of my way with you.

Thanks also to Simonetta who has always been a big support in these months. The CNR team has been a landmark for me.